Integrated assessment models overestimate carbon removal from enhanced weathering

Tyler Kukla[1,*], Jay Fuhrman[2,3], Zach Perzan[1,4], Connor Mack[5], and Freya Chay[1]

[1]CarbonPlan, San Francisco, CA, USA
[2]Joint Global Change Research Institute, Pacific Northwest National Laboratory, USA
[3]Center for Global Sustainability, University of Maryland, USA
[4]Department of Geoscience, University of Nevada, Las Vegas, USA
[5]Scripps Institution of Oceanography, University of California San Diego, USA
[*]Corresponding author: tyler@carbonplan.org

Abstract

Enhanced rock weathering (ERW) is increasingly being included in the integrated assessment models (IAMs) that inform climate policy debates. The first generation of ERW modules simplifies geochemistry considerably, and in ways that could overestimate projected carbon dioxide removal (CDR). For example, they assume that all dissolved rock becomes carbon removal with perfect efficiency, and that a hectare of land can support an essentially unlimited carbon removal flux. Here, we test the consequences of these simplifications. We use the rock application schedule of one IAM, GCAM, to drive a reactive transport model of soil geochemistry, SCEPTER, in a scenario that reaches 4.6 Gt of carbon removal per year by 2050. While SCEPTER broadly reproduces how much rock weathers, it does not replicate GCAM's CDR, reaching just 38 percent of GCAM's time-integrated total. The difference is owed to buffering reactions that GCAM omits, namely neutralization of soil acidity and carbonate precipitation as soils alkalize. These losses grow with the scale of global deployment because, on finite cropland, adding more rock drives soil alkalization and carbonate precipitation. They also vary with time, as soil acidity neutralizes nearly all alkalinity released in the first 10–20 years of rock spreading. This penalizes slow ERW adoption by limiting both the amount of rock spread and the fraction of rock weathering that contributes to CDR by 2100. Because these losses vary with the pace and scale of adoption, the next generation of ERW modules should represent them directly rather than with a constant correction factor. Until the science of ERW matures, IAMs should also avoid upper-bound assumptions that risk overstating ERW's role in a credible CDR portfolio.

1 Introduction

Integrated assessment models (IAMs) are responsible for some of the most optimistic estimates of enhanced weathering's (ERW) global carbon removal potential. These models often project 3–8 Gt of carbon dioxide removal (CDR) per year from ERW, and 100–400 Gt of CDR by 2100 (Chiquier et al., 2025; Fuhrman et al., 2023; Gaucher et al., 2025; Harris et al., 2026; Strefler et al., 2018, 2021). In contrast, bottom-up geochemical estimates of ERW's potential are much lower, spanning just 0.1–2 Gt of CDR per year (Baek et al., 2023; Beerling et al., 2020, 2025; Buma et al., 2026; Derry et al., 2026; Mayer et al., 2025). This paper explores how much of the gap stems from IAMs' treatment of ERW geochemistry.

IAMs couple representations of energy, land, economic, and climate systems, and they have only re-

cently begun to include ERW (Bauer et al., 2023; Gaucher et al., 2025; Morrow et al., 2023; Strefler et al., 2018). These early ERW modules simplify geochemistry, sometimes in ways that could inflate CDR. To understand how, it is helpful to consider CDR as the product of three factors: the amount of feedstock applied, the dissolution fraction, and the alkalinity export fraction. The dissolution fraction is the proportion of rock that weathers in a given time horizon, and the alkalinity export fraction is the proportion of cations released from weathering that leave the soil as alkalinity.

The dissolution fraction in IAMs is often optimistic. IAMs use fine grain sizes and fast dissolution rates occurring far from equilibrium (Bauer et al., 2023; Chiquier et al., 2022; Fuhrman et al., 2023; Merfort et al., 2025; Strefler et al., 2018). In some cases, these numbers are tuned to justify total dissolution of an arbitrarily large amount of rock in a single year (Chiquier et al., 2022; Fuhrman et al., 2023). Other models simulate lower dissolution fractions (~5–30 percent) to be more consistent with the ERW literature, but they still achieve high total CDR by assuming large feedstock application rates reaching up to 150 t ha^{-1} (Gaucher et al., 2025; Strefler et al., 2021).

The alkalinity export fraction in IAMs is also optimistic: to our knowledge, all IAMs implicitly set this number to one (Supplementary Table S1) (Chiquier et al., 2025; Fuhrman et al., 2023; Gaucher et al., 2025; Harris et al., 2026; Holz et al., 2018; Strefler et al., 2021). In reality, there are many processes that can limit alkalinity export and storage. Alkalinity can be consumed through soil acidity buffering, in which the reservoir of exchangeable and sorbed acidity in the soil is neutralized (Holden et al., 2024; Jessen et al., 2026; Kanzaki et al., 2025; Maher et al., 2026; Rogers & Maher, 2026; Su et al., 2026; Te Pas et al., 2025). It can also be taken up by secondary phases including soil carbonates and clays, especially as weathering raises the pH of soil porewaters over time (Derry et al., 2026; Steinwidder et al., 2025; Vienne et al., 2024; Vienne, Cox, et al., 2026; Wang et al., 2025). These losses can impede alkalinity export for years to decades (Jessen et al., 2026; Kanzaki et al., 2025; Maher et al., 2026) and are often cited to explain results that find little or no CDR (Hammes et al., 2025; Holden et al., 2024; Larkin et al., 2022; Te Pas et al., 2025; Vienne et al., 2024; Vienne, Frings, et al., 2026). Alkalinity export is also limited by non-carbonic acid weathering, which does not release alkalinity, and storage is constrained by re-equilibration of the carbonate system when weathering products reach the ocean (Dietzen & Rosing, 2023; Holden et al., 2024; Kanzaki et al., 2023; Renforth & Henderson, 2017). These losses are widely represented in geochemical estimates of enhanced weathering, but they remain absent from IAMs.

Since IAMs shape expectations about how to reach climate targets, it is imperative that their estimates are geochemically realistic, even without detailed process representation. Here, we test whether the

ERW results from an IAM can be reproduced in a reactive transport model that captures dissolution and alkalinity export mechanistically. We force the reactive transport model SCEPTER (Kanzaki et al., 2022, 2024) with a feedstock application schedule from the IAM GCAM (Fuhrman et al., 2023), and compare global CDR between the two models. Three results stand out. First, the alkalinity export fraction in SCEPTER is well below one. While SCEPTER broadly reproduces the dissolution fraction of GCAM's very fine feedstock (20 μm diameter), soil buffering reactions limit cumulative CDR to just 38 percent of GCAM's estimate. Coarser feedstocks that may be more realistic lower the dissolution fraction and further reduce CDR. Second, the alkalinity export fraction falls as global deployment ambition increases. Meeting GCAM's 4.6 Gt yr^{-1} target on finite cropland requires rock doses that push soils alkaline, which causes widespread carbonate precipitation. Consequently, IAMs overestimate CDR more at larger scales. Third, the alkalinity export fraction varies over time, so IAMs cannot represent it with a constant correction factor. Soil acidity consumes nearly all alkalinity in the first 10–20 years after annual rock application begins, after which the export fraction increases with time. Slower ERW adoption therefore decreases not only the volume of rock spread, but also the fraction converted to CDR by 2100.

Our results demonstrate that, by omitting key geochemical processes, the current generation of IAMs can project unrealistically high CDR volumes from ERW. Extremely high feedstock application fluxes and fine grain sizes only exacerbate the effect. We argue that the next generation of enhanced weathering modules in IAMs needs to include more realistic geochemical constraints and how they vary with the scale and rate of adoption.

2 Methods

Our analysis compares the enhanced weathering carbon removal outcomes of GCAM 5.4 (Fuhrman et al., 2023; Morrow et al., 2023) to equivalent estimates using SCEPTER v1.0.2 (Kanzaki et al., 2022, 2024), which simulates feedstock dissolution and soil buffering processes in the shallow soil (0–50 cm). We force SCEPTER to follow the rock application schedule from the GCAM simulation of Fuhrman et al. (2023) that restricts warming by 2100 to 1.5 °C. In this simulation, CDR from ERW starts at zero in 2020, reaches 4.6 Gt yr^{-1} by 2050, and sustains that rate through 2100, with rock spread across GCAM's 32 geopolitical regions (Supplementary Figure S1). We first match GCAM's application schedule with SCEPTER, and then depart from it in three ways: using coarser feedstock, lowering the global scale of deployment, and slowing ERW adoption. Each departure relaxes one element of GCAM's rock application that may be considered optimistic. We refer to the simulations that follow GCAM's deployment ceiling

(4.6 Gt yr^{-1}) as "high-scale", and we use "reduced-scale" to refer to simulations with a lower deployment ceiling (maximum 0.5 Gt yr^{-1}). We do not account for emissions from mining, crushing, transporting, and spreading rock, which are often found to be about 10–30 percent of a feedstock's potential CDR (Aviso et al., 2026; Cobo & Guillén-Gosálbez, 2026; Eufrasio et al., 2022; Li et al., 2024; Moosdorf et al., 2014; Zhang et al., 2023).

2.1 Regional SCEPTER simulations

For each GCAM region, we run enhanced weathering simulations at nine application fluxes spanning 0.1–30 t ha^{-1} yr^{-1}, and one no-amendment control. Each simulation starts from a single regional spinup run at a representative grid cell, tuned to local soil properties following Kanzaki et al. (2025) (see Supplementary text for more information). To match GCAM, the feedstock has a grain diameter of 20 µm and a roughness factor of 50, such that the specific surface area is 4.5 m^2 g^{-1} (Fuhrman et al., 2023; Strefler et al., 2018). GCAM's fine-grained feedstock weathers almost completely, whereas observed dissolution fractions are often much lower (Beerling et al., 2024; Buckingham et al., 2022; Holden et al., 2024; Suhrhoff, Dietzen, et al., 2026). We therefore repeat the regional simulations for eight grain sizes with specific surface areas spanning 0.03–4.5 m^2 g^{-1}. All simulations use a glassy basalt feedstock of Kanzaki et al. (2025), with its silica content rescaled to match GCAM's carbon removal potential of 0.3 tonnes of CDR per tonne of rock.

2.2 Scaling to regional and global CDR

GCAM specifies how much rock is spread in a given region every year, but not how it is distributed across cropland. Although ERW could be practiced elsewhere, IAMs, including GCAM, assume it occurs on cropland, where it is well-studied and practical because it can build on existing rock spreading infrastructure and may improve crop yields. We fix each region's application flux, solving for the cropland area required to match GCAM's application each year. This lets ERW grow by expanding the land area where it is practiced rather than increasing the feedstock dose each hectare receives. Whenever a region spreads more rock than the year before, we treat the new area as an application cohort: land that begins receiving rock that year and continues at the same application flux through 2100. Every cohort in a region follows the same representative simulation, offset by its start year, which allows us to use a single simulation to match any arbitrary rock application schedule (Supplementary Figure S4). We calculate regional gross CDR in year j as the sum of the CDR flux, F_{CDR}, for each cohort i, multiplied by the cohort's land area, A_i:

$$\mathrm{CDR}_j = \sum_{i=0}^{j} F_{\mathrm{CDR}}(j - t_i) \times A_i, \tag{1}$$

where t_i is the start year for cohort i and $j - t_i$ marks the cohort's age (see Supplementary text for more detail, including a description of the cohort-level CDR calculation).

We calculate global CDR by finding the application flux and grain size that maximize each region's cumulative CDR by 2100, and summing the regional CDR rates. We then repeat this selection, accounting for finite cropland area because, at low rock application fluxes, matching GCAM could require more cropland than a given region has. We calculate the fraction of cropland used for ERW in each region using the dataset of Mehrabi et al. (2024) (Supplementary Figure S5), and assume that ERW can use up to 100 percent of the available cropland, although on average only 50–60 percent appears acidic enough to benefit from rock amendment (Levy et al., 2024). When imposing the cropland area limit, each region's best CDR outcome is drawn only from application fluxes that fit within the available cropland (Supplementary Figure S6, Figure S7).

2.3 Alternative rock application schedules

We modify the high-scale rock application schedule in two ways. First, we explore how alkalinity export changes with less intense global feedstock application by rescaling it to a maximum potential CDR of 0.5 Gt yr^{-1} ("reduced-scale"), which is closer to recent estimates (Buma et al., 2026; Mayer et al., 2025). Second, we slow ERW adoption. GCAM's adoption rate is high — an exponential fit to its first decade gives a growth coefficient, k, of 0.52 yr^{-1} (doubling every 1.3 years), and a logistic fit to the full trajectory gives k=0.24 yr^{-1} (doubling every 2.9 years) — and it is already two orders of magnitude above actual ERW deployment as of June 2026 (Supplementary Figure S8). We pin each schedule to cumulative sales by 2026 (CDR.fyi, 2026), then either retain GCAM's full trajectory k or lower it after the first decade to 0.13 yr^{-1} (doubling every 5.3 years), the median of the historical technologies dataset of Nemet et al. (2023) (Supplementary Figure S9). These adjusted curves may also be considered optimistic because they keep GCAM's high near-term growth rate and treat all ERW sales as occurring in our reference year, 2026.

2.4 Sensitivity analysis

To test the sensitivity of our results to geochemical and adoption uncertainty, we ran a distance-based generalized sensitivity analysis (DGSA) on the seven GCAM regions with the highest cumulative rock application. Our analysis varies the application flux, cation exchange capacity, grain size, water infiltration rate, and the shape of the adoption curve. DGSA methods and results are described in detail in the Supplementary text (Supplementary Figure S10 to Figure S13).

3 Results

3.1 Soil buffering effects on alkalinity export

GCAM assumes that all cations released from weathering are exported as alkalinity and ultimately contribute to CDR. In SCEPTER, however, much of the alkalinity is lost to reactions that buffer changes in pH. When the dissolution fraction is high, as it is with GCAM's fine-grained feedstock, these losses control the fraction of potential CDR that is achieved, which we refer to as CDR efficiency.

Which buffer reaction dominates depends on the intensity of rock application through its control on pH (Goulding, 2016). For every point on Figure 1a, the same amount of rock is spread globally so only its concentration varies. In all cases, the dissolution fraction is high. About 90 percent of applied feedstock weathers each year, compared to 100 percent in GCAM. The alkalinity export fraction is much more variable. At very low rock application fluxes (<1 t ha^{-1} yr^{-1}), soil acidity buffering consumes most of the alkalinity released, limiting CDR. At higher application fluxes (>4 t ha^{-1} yr^{-1}) soils eventually become alkaline and soil carbonate starts to form, also consuming alkalinity. Globally, this trade-off from soil acidity buffering to soil carbonate buffering marks peak CDR efficiency, and it occurs at a fixed application flux of 2–3 t ha^{-1} yr^{-1}. A similar crossover point is found for nearly all regions (Supplementary Figure S15). Importantly, the buffering mechanism trade-off is tied to the alkalinity flux, not the application flux. If we decrease the alkalinity flux by lowering the dissolution fraction, total CDR declines and the trade-off between the soil acidity and carbonate buffered regimes shifts to a higher rock application flux (Supplementary Figure S16).

We care about CDR efficiency in part because costs and emissions rise with the amount of rock spread, so ERW projects will not be viable if efficiency is too low (Aviso et al., 2026; Cobo & Guillén-Gosálbez, 2026; Rinder & Von Hagke, 2021). Figure 1b shows that the most CDR-efficient rock application flux is less achievable in the high-scale case. On a finite amount of cropland, the high-scale case requires

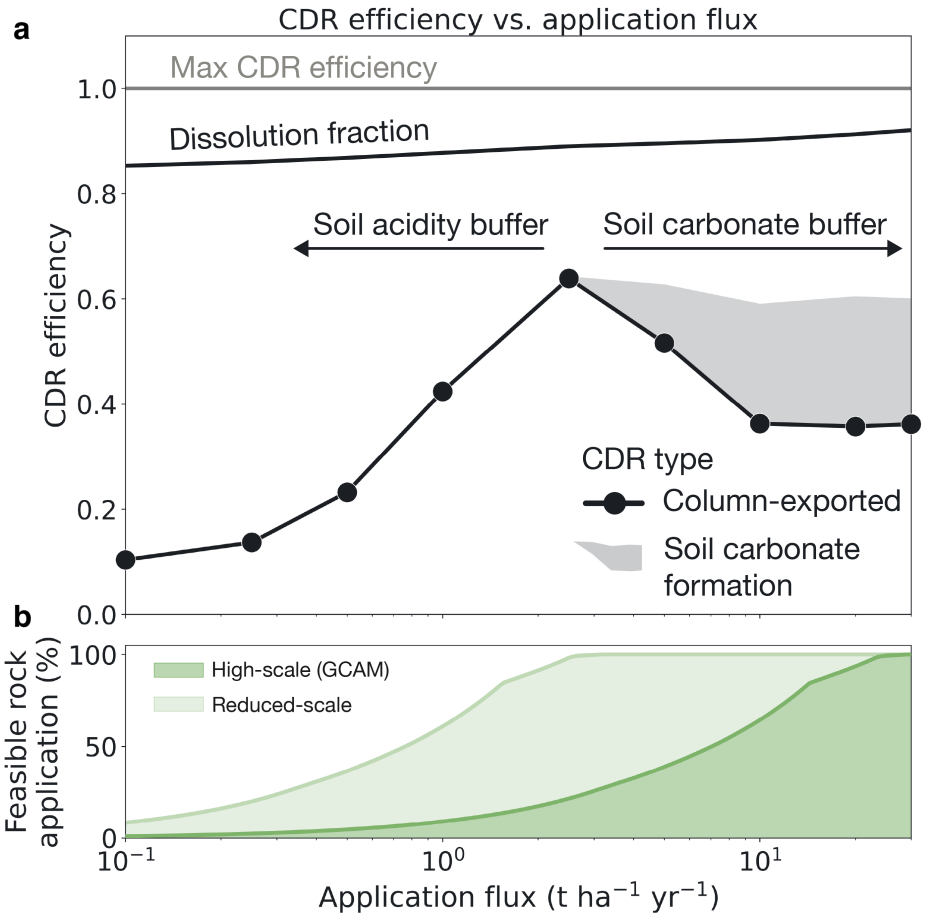


Figure 1: Time-integrated CDR efficiency depends on the feedstock application flux. (a) Global CDR is limited by neutralizing soil acidity below an application flux of 2.5 t ha^{-1} yr^{-1}, and by soil carbonate formation above it. The shaded area reflects carbon taken up by soil carbonate formation, which we do not count as durable CDR. (b) The percent of annual rock application that is feasible, assuming 100 percent of cropland can be used for ERW, for the high-scale (dark green) and reduced-scale (light green) cases. The high-scale case requires higher application fluxes to meet the more ambitious global deployment.

high application fluxes that drive soil carbonate accumulation and lower CDR efficiency (Figure 1b, dark green). The reduced-scale case, in contrast, mostly avoids widespread carbonate accumulation and permits higher CDR efficiency (Figure 1b, light green).

3.2 Limits on CDR efficiency at scale

We are unable to replicate the CDR achieved in GCAM in our SCEPTER (high-scale) simulations (Figure 2). Even when we assume unlimited cropland availability and use GCAM's feedstock diameter of 20 μm, time-integrated CDR is just 68 percent of what GCAM achieves (Figure 2a, green line). In this upper-bound case, CDR inefficiency is dominated by the soil acidity buffer, with smaller contributions from soil carbonate precipitation and incomplete dissolution (Figure 2b, "best (no land limit)"). Limiting ERW to the available cropland area forces higher rock application fluxes, widespread alkalization, and more soil carbonate accumulation that reduces CDR efficiency to 38 percent (Figure 2a,b, "best (land limit)"). If we also use a coarser feedstock (specific surface area about 0.1 m^2 g^{-1}, or roughly 100 μm diameter), the dissolution fraction declines sharply, limiting peak annual CDR to 0.8 Gt yr^{-1} and CDR efficiency to 10 percent (Figure 2a, orange line; Figure 2b, "lower surface area").

In the reduced-scale case, the cropland limit no longer pushes soils into widespread carbonate formation. The smaller global deployment permits lower rock application fluxes and higher CDR efficiency, reaching 63 percent in the land-limited case. At these lower application fluxes, acidity buffering, not carbonate precipitation, accounts for most of the alkalinity loss (Figure 2c, d).

We note that the land-limited, high-scale case, with 38 percent CDR efficiency, is more efficient than 93 percent of the simulations in our DGSA, which vary grain size, cation exchange capacity, application flux, and water infiltration rate. In more than half of our DGSA draws, CDR efficiency falls below 10 percent (Supplementary Figure S12).

Our SCEPTER simulations also shift when CDR occurs relative to GCAM. Soil acidity limits alkalinity export in SCEPTER for the first 10–20 years after rock spreading begins (Figure 2a, c). This means time-integrated CDR efficiency increases over time, particularly after the soil acidity reservoir is neutralized.

3.3 Cumulative CDR by 2100 across adoption curves

Geochemical controls on alkalinity export mean that total CDR and CDR efficiency both depend on the scale and pace of ERW adoption. Larger global deployment leads to more rock spreading and more CDR, but typically at lower efficiency, because each hectare must receive more rock. A faster pace

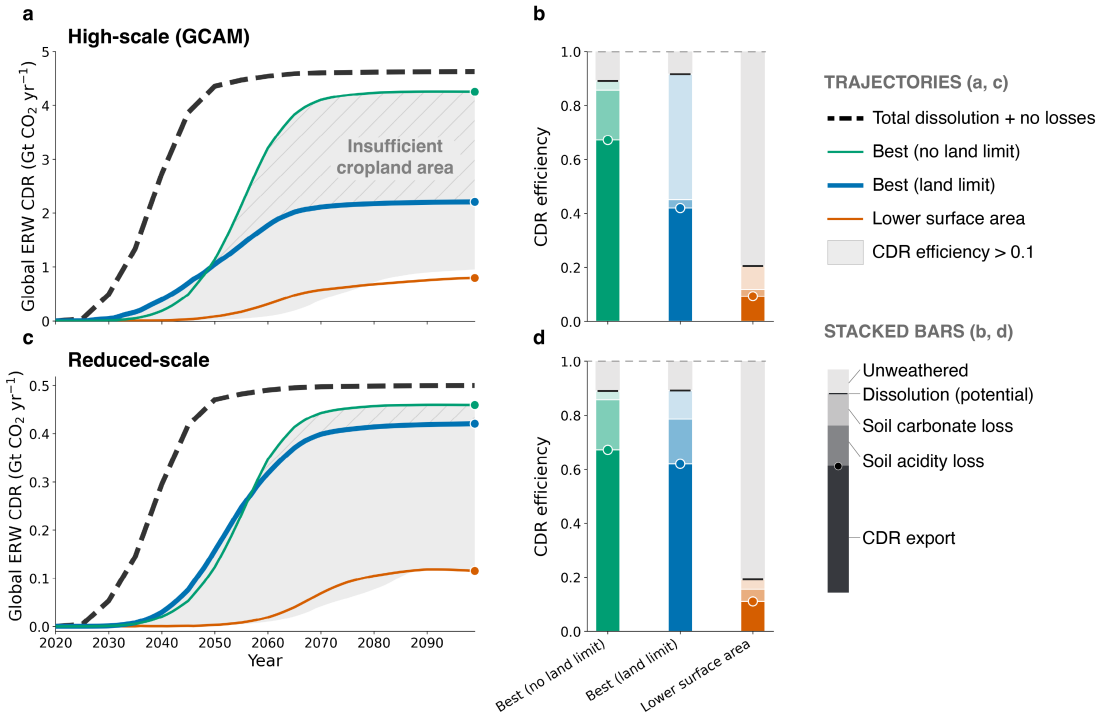


Figure 2: Reactive transport model results showing CDR from ERW over time (a, c) and CDR decomposed relative to the maximum potential CDR (b, d). Green line and dot refer to the best-case global CDR assuming no limits on the available land area. Blue line and dot assume enhanced weathering cannot use more than all of the cropland in a given GCAM region. Orange line imposes this land limit and assumes a coarser feedstock grain size of 100 µm with a roughness factor of 20, more consistent with the geochemistry literature. Gray ribbon shows the range of simulations where time-integrated CDR efficiency exceeds 10 percent, a rough proxy for the upstream emissions burden. CDR losses are dominated by soil carbonate formation in the high-scale case (a,b), and by soil acidity in the reduced-scale case (c,d).

of adoption raises CDR efficiency by raising the average age of application cohorts by 2100, so more cohorts have moved past the inefficient early stage when soil acidity is being neutralized.

These effects are illustrated in Figure 3. Following GCAM's rock application schedule (rescaled for the reduced-scale case), cumulative potential CDR by 2100 is 280 Gt in the high-scale case, and 30 Gt in the reduced-scale case. Realized CDR on finite croplands, however, is much lower, achieving 107 Gt and 19 Gt, respectively. With lower surface area feedstock, cumulative CDR declines further to 28 and 3.6 Gt, respectively, by 2100 (Figure 3).

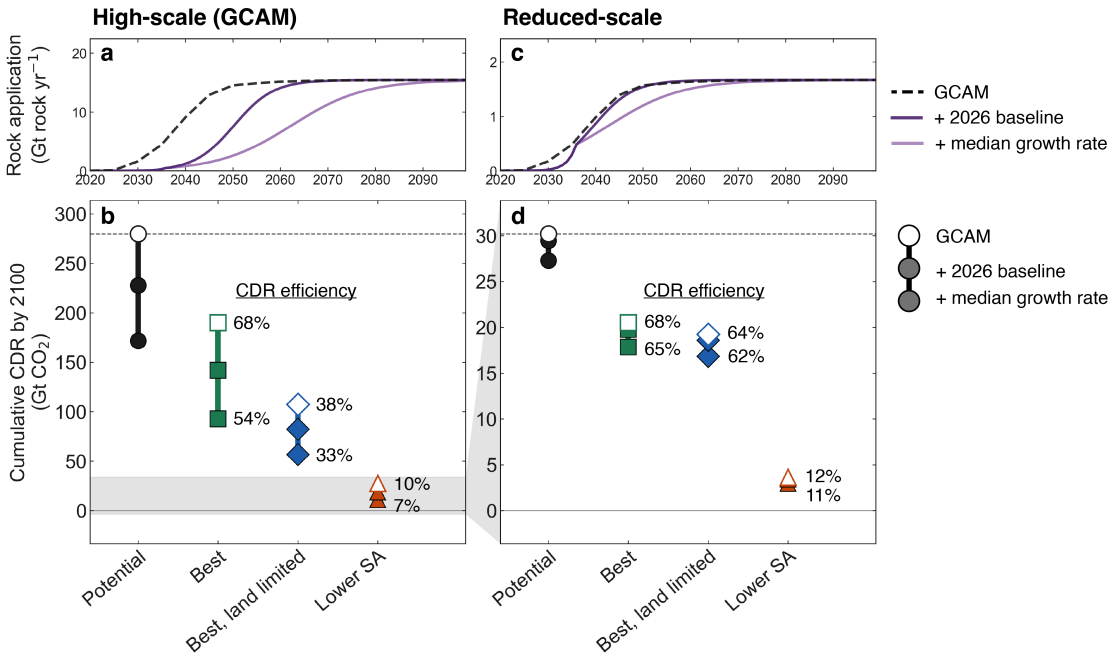


Figure 3: Cumulative CDR under different adoption scenarios. (a, c) Global rock application schedules for the high-scale case (a) and the reduced-scale case (c). The best-fit curve is then modified to be pinned to the 2026 baseline (cumulative cdr.fyi sales as of June 2026) (dark purple), and to lower k to 0.13 yr^{-1} after the initial 10-year ramp (light purple). (b, d) Cumulative CDR. Each point on a vertical line refers to a different adoption scenario. Black points show potential CDR assuming total dissolution with no losses. Green, blue, and orange points follow the same convention as Figure 2.

Slower ERW adoption further decreases CDR by 2100, especially in the high-scale case. That's because a larger global deployment requires more doubling intervals before adoption saturates. In the high-scale case, lowering k from 0.24 yr^{-1} to 0.13 yr^{-1} decreases cumulative potential CDR from 280 to 172 Gt — a 39 percent decline. Time-integrated CDR efficiency also decreases with slower adoption from 68 to 54 percent with no cropland area limit, or from 38 to 33 percent when cropland area is considered. These losses are exacerbated for less reactive feedstocks — our sensitivity analysis runs show that CDR efficiency declines by 35–70 percent per decade of delay in the temporal centroid of rock application as feedstock grains get coarser (Supplementary Figure S13). These losses in time-integrated efficiency

are lower in the reduced-scale case, largely because the slower adoption rate does not delay the timing of peak deployment as much.

4 Discussion

The first generation of IAMs to simulate ERW (Chiquier et al., 2025; Fuhrman et al., 2023; Gaucher et al., 2025; Harris et al., 2026; Holz et al., 2018; Morrow et al., 2023; Schaber et al., 2024; Strefler et al., 2021) are producing CDR estimates that may be unreasonably high. We can trace this to three oversimplifications that future work should address: alkalinity export fractions are set to one, CDR efficiency does not depend on the feedstock application intensity, and CDR efficiency is decoupled from the rate of adoption.

4.1 Perfect alkalinity export is a poor assumption

To our knowledge, all IAMs with an ERW module assume cations exit the soil as alkalinity with perfect efficiency. This assumption is widely understood to be an oversimplification, and previous IAM work has pointed out that relaxing it could lower CDR (Fuhrman et al., 2023; Strefler et al., 2018).

Our work builds on a growing number of results demonstrating that pH buffering reactions, especially soil acidity buffering, can severely limit alkalinity export for years (Derry et al., 2026; Holden et al., 2024; Jessen et al., 2026; Kanzaki et al., 2025; Maher et al., 2026; Rogers & Maher, 2026). These loss processes are too large and pervasive to ignore. Our SCEPTER simulations show that even with near-complete dissolution and unlimited cropland, roughly a quarter of alkalinity released through 2100 is lost to buffering reactions. When we restrict ERW to available cropland in the high-scale case, the alkalinity loss fraction increases to about half (Figure 2b). Importantly, which buffer is active will change over time as porewater pH rises. If modeled time horizons for alkalinity export are correct (Kanzaki et al., 2025; Maher et al., 2026), most field trials are likely still in the soil acidity buffering regime, where weathering produces dampened pH increases as soil acidity is neutralized (Beerling et al., 2024; Holden et al., 2024; Larkin et al., 2022; Maxbauer et al., 2026).

4.2 CDR efficiency depends on scale via feedstock application intensity

IAM CDR fluxes are already diverging from the geochemical literature. At the field level, IAMs often prescribe or imply CDR fluxes of 2–12 t ha^{-1} yr^{-1} (Supplementary Table S2). The GCAM simulation we analyzed here would reach 17 t ha^{-1} yr^{-1} in the highest-flux region if ERW was concentrated in half of

regional cropland (e.g., Levy et al., 2024). In contrast, a recent synthesis of geochemical estimates found a median CDR flux of 0.8 t ha^{-1} yr^{-1} (Suhrhoff, Dietzen, et al., 2026). In natural basaltic systems, strong buffering processes appear to limit carbon removal to less than 2 t ha^{-1} yr^{-1} (Derry et al., 2026). Fluxes above 2 t ha^{-1} yr^{-1} are not impossible but assuming they can be reached across global cropland requires geochemical justification.

Even if the high CDR fluxes implied by some IAM scenarios can be achieved, they might not be agronomically sustainable. Over time, intense alkalinity dosing can raise the pH of the soil too high, risking yield loss and soil carbonate formation that makes future pH management more difficult. In our simulations, the highest CDR fluxes that can be sustained without widespread carbonate formation are about 0.2–2 t ha^{-1} yr^{-1} depending on the region, or about 0.6 t ha^{-1} yr^{-1} in the global mean (Supplementary Figure S17). IAMs could bring their CDR fluxes into this range by using lower effective dissolution rates or coarser grains, both of which have support in the geochemical literature (Anand et al., 2026; Renforth et al., 2015; Suhrhoff, Reinhard, et al., 2026). Just limiting the maximum scale volume is not sufficient on its own, however, because if CDR efficiency remains too high the model will still underestimate the cost and emissions per tonne of CDR.

ERW scale estimates also require defining the amount of eligible cropland, which sets the feedstock application intensity needed to meet a global deployment target (e.g., Figure 1). Some models have assumed that 30–75 percent of global croplands are used (Gaucher et al., 2025; Tu et al., 2026). Others, including GCAM, do not impose an explicit limit, but would require high rock application fluxes even if all cropland is used (Supplementary Table S2). We suggest that half of global cropland should serve as an upper limit on ERW adoption, since that is roughly the fraction considered acidic enough to benefit from ERW (Levy et al., 2024). We did not follow this guidance here because GCAM does not impose a cropland area limit, and we wanted to provide a conservative estimate of the effect of limited area on CDR efficiency.

If we keep CDR fluxes below the carbonate precipitation threshold and limit ERW to half of global croplands, we estimate a maximum scale capacity of about 0.6 Gt yr^{-1} and 26 Gt of cumulative CDR by 2100 (Supplementary Figure S18, Figure S19). This is a rough estimate because it collapses spatial variability to GCAM's 32 regions, but it is consistent with a recent global estimate based on the alkalinity "carrying capacity" of agricultural soil water (Mayer et al., 2025).

4.3 ERW adoption rate affects the evolution of alkalinity export

Alkalinity export is expected to be lowest in the first years of rock spreading, and increase over time as the soil acidity reservoir is neutralized. All else equal, this means that older rock application cohorts tend to have higher time-integrated CDR *and* CDR efficiency. Over a given time horizon, the pace of ERW adoption therefore influences the fraction of weathering that contributes to CDR.

Given this link to alkalinity export, IAMs should push toward adoption rate constraints that are more clearly justified, perhaps by comparison to technological analogs (Nemet et al., 2023; Tu et al., 2026). Our results show that GCAM's rapid adoption raises the CDR efficiency of ERW (Figure 3; Supplementary Figure S13). Other IAMs and global models show similarly fast growth before reaching their deployment ceilings (Supplementary Figure S21). These rates are on the upper end of adoption rates for historical technologies (Nemet et al., 2023). In contrast, some of the latest IAM results, including new GCAM runs, impose a 20 percent per year limit on enhanced weathering adoption (Chadsey et al., 2026; Harris et al., 2026). Recent work using agricultural technologies as an analog for enhanced rock weathering adoption predicts growth coefficients of about 0.16–0.23 yr^{-1} (doubling every 3.0–4.3 years) (Tu et al., 2026) (Supplementary Figure S22).

The timing of rock application also affects how we characterize ERW losses. For example, we treat soil carbonate formation and soil acidity neutralization as losses, although the enhanced weathering literature sometimes frames them as "lags" (Beerling et al., 2024, 2025; Hasemer et al., 2024; Kanzaki et al., 2025; Reershemius et al., 2023; Steinwidder et al., 2025). The lag framework is defensible — these losses may be reversed when the soil reacidifies (Kanzaki et al., 2025), though reversal is not guaranteed (Derry et al., 2026; Holden et al., 2024; Su et al., 2026). Moreover, reacidification also restores a soil's buffering capacity, which will limit alkalinity export from future rock amendment. In our simulations, soils are not given the chance to reacidify: once rock spreading starts, it continues through 2100. We expect that this choice increases CDR. Soil reacidification can take years (Chambers & Garwood, 1998; Cifu et al., 2004; Guo et al., 2010; Helyar et al., 1990; Long et al., 2015; Taylor et al., 2021), so ceasing rock application to recover the lost alkalinity likely drives less CDR than just continuing to apply rock every year without reversing the loss.

Finally, strategically varying rock application rates over time could shorten the time required to neutralize soil acidity. While we use a constant application flux, a dynamic schedule could apply rock intensely in the near term to overcome the soil acidity reservoir quickly, then less intensely to limit soil carbonate formation. These front-loaded applications would require careful management to avoid topsoil alkaliza-

tion. We leave the task of balancing topsoil pH with optimal rates of subsoil acidity neutralization for future work.

4.4 Toward geochemically grounded ERW estimates in IAMs

IAM-based estimates of ERW's potential should better reflect primary geochemical constraints beyond feedstock dissolution — especially soil acidity buffering and carbonate precipitation. Ignoring these processes risks inflating ERW estimates. A constant correction factor could make estimates more realistic, but it would miss how alkalinity export varies with the pace and scale of ERW adoption. In contrast, embedding a full reactive transport model would introduce unnecessary complexity and computational cost.

We see two main paths forward to capture key geochemical processes and how they interact with global ERW adoption. IAMs could combine empirical estimates of a soil's buffering capacity with a carbonate system solver (Mayer et al., 2025; Nelson & Su, 2010; Rogers & Maher, 2026). That would make alkalinity export more realistic, but it would still omit some processes that can affect CDR outcomes, such as plant cation uptake or non-carbonic acid weathering. A more intensive solution would be to build a reactive transport model emulator to capture a wider range of processes in a computationally efficient framework. Both of these solutions, especially an emulator, require some upfront work, but they would help close the gap between IAMs and process-based model estimates of ERW.

4.5 Limitations

Our analysis offers a more geochemically nuanced treatment of ERW at scale than IAM formulations. But it still includes assumptions, some of which could lead to optimistic CDR estimates, that should be stress-tested in future work. Our reaction network omits certain alkalinity sinks for simplicity, such as aluminum hydrolysis and plant cation uptake. We also force simulations with precipitation rather than runoff, and long-term mean climate forcing rather than event-scale forcing, to give an upper bound on water-rock interaction and export, and to limit secondary calcite formation (Clow & Mast, 2010; Gaillardet et al., 2019). Our simulations also only span a half-meter of soil, but the soil acidity reservoir can extend much deeper, requiring more alkalinity to neutralize it (Jessen et al., 2026; Maher et al., 2026; Rogers & Maher, 2026). Finally, we impose no agronomic limits on rock dosing, allowing soils to become highly alkaline — CDR-weighted porewater pH reaches about 8.9 in the high-scale case, or 7.9 in the reduced-scale case. These high pH levels permit higher CDR fluxes, but they could also bring adverse agronomic consequences, including micronutrient deficiencies and disease risk (Fageria & Baligar, 2008;

Haynes, 1984; Levy et al., 2024; Parker & Walker, 1986).

5 Conclusion

Integrated assessment modelers have taken on the difficult task of incorporating ERW into their models while its evidence base is still evolving. A lag between the state of ERW science and its representation in IAMs is inevitable. As modelers push toward the next generation of ERW modules, they should aim for dissolution and alkalinity export parameterizations that are more firmly grounded in the literature and plausibly agronomically sustainable over decades. The current models are not there yet, and are biased toward the upper bound of potential CDR.

Inflated CDR projections carry risk: they overstate society's capacity to defer emissions reductions and neutralize residual emissions (Bindl et al., 2025; Schaber et al., 2024; Shindell & Rogelj, 2025). This risk extends beyond ERW. Similar concerns have been raised about over-reliance on bio-energy with carbon capture and storage, or BECCS, in IAMs (Anderson & Peters, 2016; Deprez et al., 2024; Smith et al., 2016). ERW was added to some IAMs to reduce that reliance (Chiquier et al., 2025; Gaucher et al., 2025; Strefler et al., 2021), though our results suggest its capacity to do so has been overstated. Credible CDR portfolios therefore require prudence within each pathway at least as much as they require a diversity of pathways. While the science is still developing, that prudence means avoiding upper bounds that are likely to err high in favor of more conservative parameterizations. Underestimates can be revised upward as confidence improves, but overestimates risk decoupling expectations and investment from what CDR pathways can actually achieve.

Acknowledgements

We are grateful for feedback from Grayson Badgley and Chris Allen that improved the manuscript. Tyler Kukla thanks Raphael Hagen for software support. Tyler Kukla, Zach Perzan, and Freya Chay were supported in part by a grant to CarbonPlan from the Chan Zuckerberg Initiative DAF, an advised fund of Silicon Valley Community Foundation.

Conflict of interest

The authors declare no competing interests.

Data availability

Results from all SCEPTER simulations described here are available on Zenodo (Kukla, 2026c). Code to run SCEPTER v1.0.2 is adapted from Kanzaki & Reinhard (2025) and is available on GitHub (Kukla, 2026b), alongside code to reproduce our analysis (Kukla, 2026a). The compiled ERW scale estimates presented in the supplement and discussed in the main text are available on Zenodo (Kukla, 2026d).

Supporting Information

S1 ERW in IAMs

Here, we briefly review how ERW is formulated in IAMs with a broad focus on geochemical and land process representation (Table S1). Notes on land process representation specifically refer to the ERW module, whereas other modules in the same model may treat land resolution, or land area limits, differently.

We also convert ERW scale estimates in IAMs to their implied CDR fluxes (Table S2). Here, we are interested in the highest modeled fluxes, since these will best approximate the upper limits we scrutinize. For every model in each paper, we pull the scenario resulting in the largest annual CDR rate due to ERW. We then convert the CDR rate (t yr^{-1}) into a flux (t ha^{-1} yr^{-1}) for every model region by dividing by the region's cropland area. We use the model's own cropland area constraints when possible. Otherwise, we use the cropland data of Mehrabi et al. (2024) and assume that 50 percent of available cropland is eligible for ERW (Levy et al., 2024). We report two CDR flux metrics: a global CDR flux weighted by each region's cumulative CDR ("CDR-weighted flux"), and the highest regional CDR flux ("Highest-region flux") (Table S2). "SoCDR" refers to ERW projections from the eighth chapter of the State of CDR report (third edition; Gidden et al. (2026)). For cases where only a single region or global value is reported (including SoCDR), the CDR-weighted and highest region fluxes are necessarily the same.

Model	Dissolution	Alkalinity export	Cropland area limit	References	Notes
GCAM	Tuned for total dissolution in one year	Total export, no losses	None	(Chadsey et al., 2026; Fuhrman et al., 2023; Javadi et al., 2026; Motlaghzadeh et al., 2025)	The same ERW geochemistry is used across all GCAM versions in the referenced papers.
REMIND-MAgPIE	Climate-dependent weathering rate of a constant 150 t ha^{-1} stock	Total export, no losses	Yes (humid and temperate treated separately)	(Bauer et al., 2023; Harris et al., 2026; Merfort et al., 2025; Strefler et al., 2021)	
C-ROADS + En-ROADS	NA	Total export, no losses	None	(Holz et al., 2018)	ERW is calculated from a global maximum capacity and a time-variable deployment percent.
GET-ACC2	About 13 percent of a fixed 150 t ha^{-1} basalt stock weathers per year	Total export, no losses	Yes (7.9 Mkm^2)	(Gaucher et al., 2025)	Inorganic and organic CDR are reported for ERW; we refer to just the inorganic results for consistency across models.
EPPA	Tuned for total dissolution in one year; fixed 20 t ha^{-1} yr^{-1} basalt application flux	Total export, no losses	No clear limit; required area can be computed from the fixed application flux of 20 t ha^{-1} yr^{-1}	(Chiquier et al., 2025)	
SCORE	NA	Total export, no losses	None	(Schaber et al., 2024)	ERW is calculated from a global maximum annual and cumulative capacity; capacity grows linearly from zero.
Tu et al. 2026	Climate-dependent weathering rate adjusted from a reference CDR flux of 1.5 t ha^{-1} yr^{-1}	Total export, no losses	Yes (50% or 75% of global cropland)	(Tu et al., 2026)	Feedstock dissolution is not explicitly modeled, but the model implicitly assumes 10 t ha^{-1} of olivine application.

Table S1: Enhanced weathering representations in IAMs and similar global-scale models. “NA” indicates feedstock dissolution is not modeled. ERW results have been reported for other IAMs in a preprint (Harris et al., 2026) (WITCH, IMAGE, MESSAGE) or the 3rd State of CDR report (Gidden et al., 2026) (AIM), but these documents did not include enough information to confidently state how ERW is treated in those models.

Reference	Model	Scenario	Peak year	Peak ERW CDR (Gt CO_2 yr^{-1})	CDR-weighted flux (t CO_2 ha^{-1} yr^{-1})	Highest-region flux (t CO_2 ha^{-1} yr^{-1})	Area basis
Chiquier et al. (2025)	EPPA	CDR Portfolio	2070	8.14	10.96	10.96	50% of world cropland
Ampah et al. (2024)	GCAM-TJU	HIGH	2050	2.15	10.48	13.86	50% of cropland, 11 GCAM regions
Fuhrman et al. (2023)	GCAM-CDR	exe_lowCCS1p5	2100	4.65	9.61	17.02	50% of cropland, 32 GCAM regions
Chadsey et al. (2026)	GCAM 7.4	Full Trade no biochar	2085	4.63	9.60	16.96	50% of cropland, 32 GCAM regions
Fuhrman et al. (2024)	GCAM 6.0	gcam-1p5	2100	2.88	8.00	13.93	50% of cropland, 32 GCAM regions
Bauer et al. (2023)	REMIND	overshoot3_Budg600-fullOvershoot	2090	4.96	7.12	8.24	REMIND ERW cropland, 12 REMIND regions
Merfort et al. (2025)	REMIND-MAGPIE	SepMark_12	2060	4.79	7.12	8.24	REMIND ERW cropland, 12 REMIND regions
Strefler et al. (2021)	REMIND-MAgPIE	C_SSP2-900-EW-only-RefAff-Const2045	2045	4.77	7.10	8.24	REMIND ERW cropland, 12 REMIND regions
Schaber et al. (2024)	SCORE	bet_1path_avg_NETs_T15_lo-MAC_optNETs	2100	5.00	6.73	6.73	50% of world cropland
Javadi et al. (2026)	GCAM-USA	HCDR	2040	0.328	6.41	16.96	50% of cropland, 49 US states
Gaucher et al. (2025)	GET-ACC2	1.5°C with high overshoot / EW on CL	2090	4.42	5.59	5.59	stated area, 7.9 Mkm^2
Motlaghzadeh et al. (2025)	GCAM-CDR	EPC1.5Q_NoBioImp_LimDAC	2085	0.0880	2.21	2.21	100% of Canada cropland
SoCDR-GCAM-China 2026	GCAM China CDR v7	Highest Ambition	2050	1.24	9.24	9.24	100% of China cropland
SoCDR-AIM 2026	AIM 3.0	Delayed Ambition	2100	4.95	6.66	6.66	50% of world cropland
SoCDR-GCAM 2026	GCAM 8.2	Delayed Ambition	2100	4.00	5.39	5.39	50% of world cropland
SoCDR-REMIND-MAgPIE 2026	REMIND-MAgPIE 3.5-4.11	Delayed Ambition	2100	2.48	3.14	3.14	REMIND ERW cropland, 7.9 Mkm^2
SoCDR-WITCH 2026	WITCH 6.0	Delayed Ambition	2100	2.26	3.05	3.05	50% of world cropland
SoCDR-MESSAGEix-GLOBIOM 2026	MESSAGEix-GLOBIOM 2.1-R12	Highest Ambition	2100	1.88	2.54	2.54	50% of world cropland
SoCDR-IMAGE 2026	IMAGE 3.4	Delayed Ambition	2100	1.80	2.43	2.43	50% of world cropland
SoCDR-OPEN-PROM 2026	OPEN-PROM 2.0	Highest Ambition	2100	0.199	0.27	0.27	50% of world cropland
SoCDR-GCAM-USA 2026	GCAM-USA 7.1 SoCDR	Highest Ambition	2050	0.0274	0.17	0.17	100% of USA cropland

Table S2: ERW carbon dioxide removal (CDR) in the peak year of each model's highest-ERW scenario in each study. Fluxes are regional CDR divided by area; the CDR-weighted flux is weighted by each region's contribution to total CDR, and the highest-region flux the maximum CDR flux. Area is 50% of each model region's 2015 cropland (Mehrabi et al., 2024) unless the study states its treated area. Models that report only one region use all of that region's cropland. REMIND models use REMIND's ERW cropland by region (Strefler et al., 2021).

S2 Calculating CDR from SCEPTER results

We define CDR in our SCEPTER simulations as excess carbonate alkalinity exported from the modeled soil column compared to a no-amendment control simulation. The mass balance of the advected flux, F_{adv} (mol m^{-2} yr^{-1}), for any species in SCEPTER can be written as:

$$F_{\text{adv}} = -F_{\text{org}} - F_{\text{inorg}} - F_{\text{dif}} - F_{\text{S}} \tag{S1}$$

where negative values indicate a flux *into* the soil column, subscripts `org` and `inorg` refer to the contribution from respired organic matter and dissolved carbonate species, respectively, `dif` refers to the diffusion flux out the top of the soil column, and S refers to the time-derivative of the mass of carbon stored in the soil column itself.

Carbon removal, $R(t)$, is calculated based on cumulative values of flux i where

$$\Phi_i(t) = \int_0^t F_i \, \mathrm{d}t'. \tag{S2}$$

Cumulative removal is then calculated as the change in the carbonate alkalinity advected flux in the amended case (`case`) compared to the control (`ctrl`), minus any contribution from fossil carbon released due to inorganic carbonate weathering:

$$R(t) = \left[\Phi_{\text{adv}}(t) + \text{MIN}\left(\Phi_{\text{inorg}}(t),\, 0\right)\right]_{\text{case}} - \left[\Phi_{\text{adv}}(t) + \text{MIN}\left(\Phi_{\text{inorg}}(t),\, 0\right)\right]_{\text{ctrl}}. \tag{S3}$$

Importantly, F_{inorg} and Φ_{inorg} refer only to the carbon derived from inorganic minerals, not any additional carbon charge balanced by the cations released from carbonate weathering. Written this way, soil carbonate precipitation (positive Φ_{inorg}) above the control case is not counted as CDR. Net carbonate dissolution (negative Φ_{inorg}) compared to the control will tend to raise CDR, decreasing Φ_{adv} by two units and Φ_{inorg} by one.

S3 SCEPTER spinup simulations

We run one spinup simulation per GCAM region based on input data at a single, representative grid cell. The representative cell minimizes the euclidean distance between its values and the cropland

area weighted regional mean across eight input variables (Table S3). For two of these variables, water infiltration rate and porewater pH, we impose bounds and filter out candidates that sit outside them. Water infiltration is forced to be greater than 0.1 m yr^{-1}, offering a conservative estimate of water-rock interaction. Initial porewater pH is restricted to 5.5–7, which removes very acidic sites where aluminum hydrolysis plays a key role in the acid base balance, as well as more basic sites that are more likely to be near or at calcite saturation.

Our spinup methods follow Kanzaki et al. (2025). Simulations are run for 10,000 years to initialize a 0.5 m deep soil profile. Four variables are given target values (Table S3) and we iteratively tune four parameters to match the targets (Supplementary Figure S2, Figure S3). The tunable parameters are the organic carbon turnover time, the input flux of organic carbon, the dissolved Ca^{2+} concentration at the top of the column (representing background weathering or historical liming), and an apparent equilibrium constant for cation exchange ($K_{H/Na}$) which the other equilibrium constants are pinned to.

Variable	Units	Bounds	Range	Role	Data source
Water infiltration rate	m yr^{-1}	≥ 0.1	0.5–2.5	Forcing	ERA5
Mean annual soil temperature	°C	NA	4.5–28.7	Forcing	ERA5
Soil moisture	m^3 m^{-3}	NA	0.16–0.36	Forcing	ERA5
Cation exchange capacity	cmol kg^{-1}	NA	9.1–39.5	Forcing	SoilGrids 2.0
Porewater pH	—	[5.5, 7.0]	5.5–6.8	Target	SoilGrids 2.0
Soil CO_2	$\log_{10}$(atm)	NA	-2.53 to -1.97	Target	MODIS, ERA5
Soil organic matter	wt%	NA	1.0–6.6	Target	SoilGrids 2.0
Exchangeable acidity	% CEC	NA	10.0–75.0	Target	WISE30sec

Table S3: Data inputs for model spinup. Water infiltration rate uses total precipitation ("tp") from ERA5 to achieve a conservative (upper-bound) estimate of water-rock interaction. Temperature is taken from the first level of ERA5's soil temperature variable ("stl1_K"). Soil moisture is the depth-weighted average of ERA5's three soil water depth levels ("swvl*"). Cation exchange capacity is taken as the mean value from 5-30 cm of the SoilGrids data, and porewater pH is taken as the value from the 15-30 cm depth level. Soil CO_2 is calculated from net primary productivity (MODIS) and temperature (ERA5). Soil organic matter is taken as the depth-weighted mean of the top 30 cm. Exchangeable acidity is taken as one minus base saturation in the top 20 cm of the soil. Data source references: ERA5 (Hersbach et al., 2020; Hersbach et al., 2023); SoilGrids 2.0 (Poggio et al., 2021); MODIS (Zhao et al., 2005; Zhao & Running, 2010); WISE30sec (Batjes, 2016).

Soil CO_2 is the only spinup forcing or target parameter that must be derived from input datasets. We calculate soil CO_2, pCO_2^{soil}, based on net primary productivity (from MODIS), NPP (g C m^{-2} yr^{-1}), and soil temperature (from ERA5), T_{soil} (K), following the approach of Gwiazda & Broecker (1994) as adopted in Gaillardet et al. (2019), Goddéris et al. (2010), and Zeng et al. (2022) (Equation S4).

$$\mathrm{pCO}_2^{\mathrm{soil}} = \mathrm{pCO}_2^{\mathrm{atm}} + \frac{A\, f_{\mathrm{NPP}}\, \mathrm{NPP}}{T_{\mathrm{soil}}^2} \tag{S4}$$

In Equation S4, $\mathrm{pCO}_2^{\mathrm{atm}}$ is the atmospheric CO_2 level set to 420 ppmv, A is a constant set to 1.03×10^6, f_{NPP} is the fraction of total NPP that contributes to CO_2 production at the mean root depth. The modeled soil CO_2 level is meant to reflect the maximum CO_2 level in the soil profile.

S4 Scaling a representative ERW simulation to a regional estimate

To conduct global ERW simulations at a reasonable computational cost, we scale up one representative ERW simulation per region to compute regional and global CDR rates. The representative simulation's results are fluxes, so we need to multiply them by an area to convert to rates. We do this by treating each year's increase in regional rock application as a new application cohort. Once started, each cohort continues at the same constant rock application flux until 2100.

Each cohort, i, is assigned a land area, A, based on the mass of new rock spread in a region beyond what existing cohorts supply, M_{new}, and the fixed rock application flux, F_{rock} (Equation S5):

$$A_{\mathrm{i}} = \frac{M_{\mathrm{new,j}}}{F_{\mathrm{rock}}} \tag{S5}$$

where j denotes the year. The mass of new rock is taken as the total mass of rock spread in the target application schedule for that region in a given year, minus the rock supplied from existing cohorts, $M_{\mathrm{i,j}}$ (Equation S6):

$$M_{\mathrm{new,j}} = M_{\mathrm{GCAM,j}} - \sum_{i=0}^{n} M_{i,j}. \tag{S6}$$

Since GCAM's regional rock application schedules are almost perfectly monotonically increasing, this approach ensures that M_{new} is always positive so long as the representative simulation's application flux is constant.

S5 Distance-based generalized sensitivity analysis (DGSA)

DGSA is a global sensitivity analysis (SA) method (Fenwick et al., 2014; Park et al., 2016) that has recently been adapted for reactive transport modeling (Maher et al., 2026; Perzan et al., 2021; Perzan & Maher, 2024). It is especially useful because it lowers the computational burden compared to other global SA methods; it considers non-scalar, multivariate response variables; and it can capture non-monotonic and threshold behavior. Our analysis uses the pyDGSA package (v1.1.1) (Perzan et al., 2021; Perzan, 2026) to conduct the DGSA in two steps.

First, we cluster simulations by response variable. We start by calculating the pairwise Euclidean distance between the multidimensional response ensemble, which serves as a measure of the difference between responses. We then use k-medoids clustering on the pairwise distance matrix to group simulations into clusters. Each cluster represents a set of simulations that behaved similarly, with no reference to the parameters that produced it. These clusters are used as inputs to the next step.

Second, for each response variable, we compare the distribution of values in a cluster to the prior sample distribution. We calculate the area between the two resulting CDFs, and then normalize it by the 95th percentile of the area obtained when cluster membership is assumed to be random and independent of the parameter value. The independent CDF distribution is estimated by a bootstrap procedure that repeatedly draws random clusters of the same size. The resulting statistic is dimensionless and centered on one. Above one, the parameter can be said to influence a simulation's behavior. Below one, it does not.

In this second step, DGSA can also be used to calculate two-way parameter interaction effects: the effect of one parameter when a second parameter is held within a specific range. To calculate the effect of parameter A conditioned on B, parameter B is binned into quantiles. The cluster-conditional CDF of parameter A is then compared to its cluster-conditional CDF additionally conditioned on the level of parameter B. As with the main effects calculation above, a bootstrapping procedure is used to test the statistical significance of the distance between CDFs.

We apply this DGSA approach to two sets of simulations. The first is our "fixed schedule" runs, which assumes a single rock application schedule (the high-scale schedule) and only varies geochemical inputs, described below. The second is our "multi-schedule" runs. It takes the same geochemical simulations from the first set, and layers on different enhanced weathering adoption curves. We treat these separately for presentation purposes, so it is easier to evaluate the geochemical effects either indepen-

dent of, or alongside ERW adoption trajectories. The fixed schedule runs are analyzed using 4 clusters, and the multi-schedule runs use 6 clusters, which results in an average of 62 and 500 simulations per cluster, respectively. When calculating interaction effects, we use four bins for the multi schedule runs, and three for the fixed schedule, selected such that each bin-cluster had enough simulations to resolve a CDF (>10). Some clusters are too sparse, yielding indeterminate results, and are not reported.

S5.1 Model configuration and parameter sampling

We run the DGSA on seven of GCAM's 32 regions to make the task more computationally feasible. We chose the seven regions with the highest cumulative rock application — Brazil, China, EU-15, India, South Asia, Southeast Asia, and the USA. These regions account for over 85 percent of global CDR in GCAM and in our own simulations.

For the fixed schedule DGSA, we used 250 draws of a Latin hypercube sampler to sample across four input parameters (Table S4). Two variables are given a log-uniform prior distribution — the dust radius and infiltration factor — such that higher values do not dominate the sensitivity.

Parameter	Units	Prior distribution	Range
Application flux	t ha^{-1} yr^{-1}	uniform	0.2–20
CEC factor	[-]	uniform	0.1–4
Dust radius	μm	log-uniform	0.33–25
Infiltration factor	[-]	log-uniform	0.25–4

Table S4: Prior input parameter ranges used in the Latin hypercube sampling step. The CEC factor is the factor change in the modeled cation exchange capacity. The dust radius sets the initial specific surface area of the feedstock assuming a roughness factor of one (this range is equivalent to a range of 3-250 using a roughness factor of 10). The infiltration factor is the factor change in the mean annual water infiltration rate. The CEC factor and infiltration factor are applied equally to the unamended control and feedstock-amended enhanced weathering simulation.

The multi-schedule DGSA considers three additional parameters that vary the rock application schedule (Table S5). These parameters have no effect on the SCEPTER results, but they influence how those results are scaled to reach regional and global CDR estimates. We again use a Latin hypercube sampler to sample 12 draws of the parameters in Table S5 for each of the 250 draws mentioned above, for a total of 3000 runs.

The parameters in Table S5 help define a logistic growth curve of the form (Equation S7):

Parameter	Units	Prior distribution	Range
C_0/L	[-]	log-uniform	5×10^{-6}–5×10^{-2}
k	yr^{-1}	uniform	0.025–0.25
L	Mt CO_2 yr^{-1}	log-uniform	2×10^{2}–5×10^{3}

Table S5: Prior input parameter ranges used in the Latin hypercube sampling step for generating rock adoption curves. C_0/L is a metric for the distance between the reference capacity and the maximum capacity — it sets the number of doubling periods required to reach L.

$$C(t) = \frac{L}{1 + (L/C_0 - 1)\, e^{-k(t-t_0)}}. \tag{S7}$$

Here, C is the global amount of rock spread in year t, k is the logistic growth coefficient, L is the saturation capacity, and t_0 is a reference year, fixed at 2026, defining the time when the reference capacity, C_0, is reached. See how they affect adoption curves in Figure S14. The bounds in Table S5 were set to bracket the high-scale and reduced-scale schedules.

We note that our sensitivity analysis approach does not impose a cropland area limit. Rock is spread at the sampled application flux to match the defined rock application schedule for each region. Some simulations end up exceeding the available cropland area in a region.

S5.2 Response variables

We use five different response variables across our fixed and multi-schedule DGSA runs. These include cumulative CDR, CDR efficiency, dissolution fraction, alkalinity export fraction, and CDR lag (Table S6). Cumulative CDR is a time series, while the other four variables are single values integrated through 2100. With a fixed rock application schedule, potential CDR is the same in every run so cumulative CDR is equivalent to the CDR efficiency — we therefore only analyze cumulative CDR in the multi-schedule DGSA. CDR efficiency is defined as the realized CDR divided by the total potential CDR (assuming total dissolution with no losses). Dissolution fraction is the fraction of total applied feedstock that dissolves. Alkalinity export fraction is the fraction of cations released by weathering that are exported from the modeled soil column. CDR lag is the number of years between when cumulative potential CDR of the applied rock and realized cumulative CDR each reach 50 percent of realized cumulative CDR by 2100.

Response variable	Units	Dimensions	DGSA
Cumulative CDR	Gt CO_2	time	multi-schedule
CDR efficiency	[-]	[-]	both
Dissolution fraction	[-]	[-]	both
Alkalinity export fraction	[-]	[-]	both
CDR lag	yr	[-]	both

Table S6: DGSA response variables. Cumulative CDR was not considered in the fixed schedule DGSA because it is functionally equivalent to CDR efficiency as long as the CDR schedule itself does not change. All responses except the CDR lag are $\log_{10}$-transformed before clustering.

S6 Supporting Figures

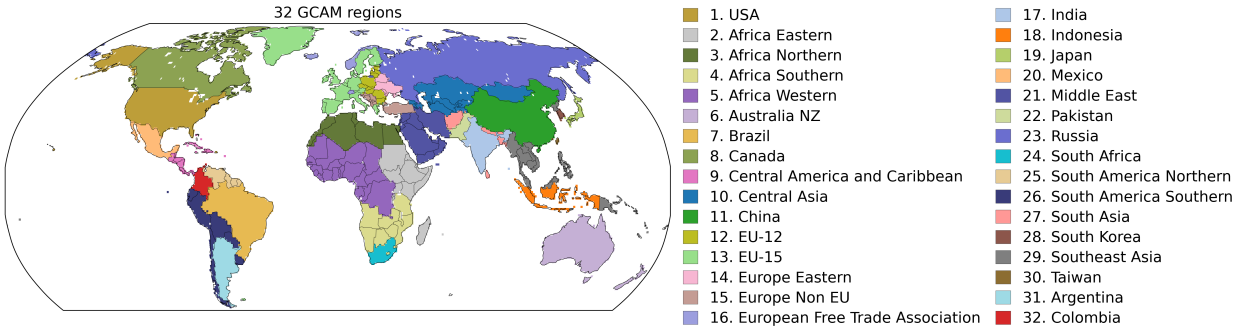


Figure S1: GCAM's 32 geopolitical regions. These regions define the rock spreading regions used in our reactive transport model simulations.

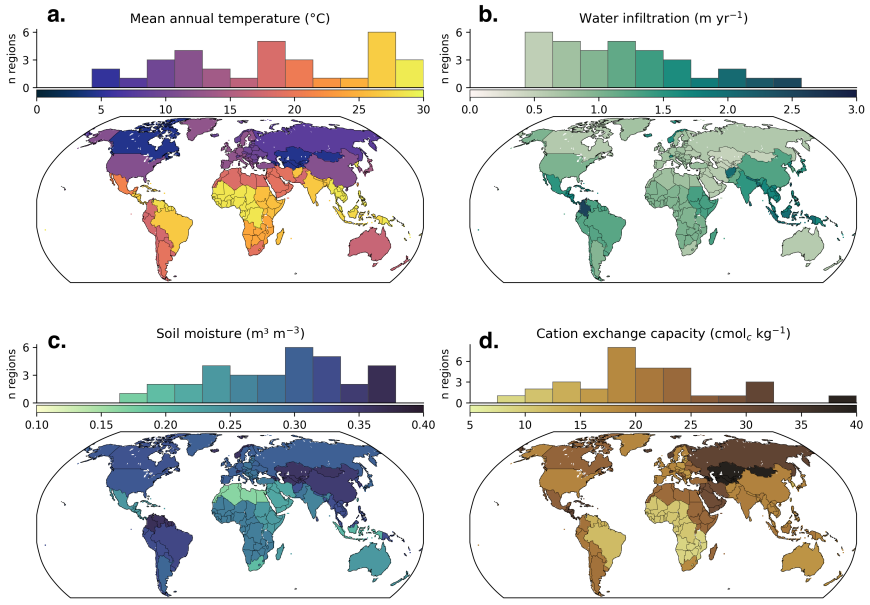


Figure S2: Spinup forcings by GCAM region. (a) Mean annual temperature; (b) Water infiltration rate (set equal to mean annual precipitation); (c) Soil moisture; (d) Cation exchange capacity. Each region gets the value of the representative cropland cell (see Methods).

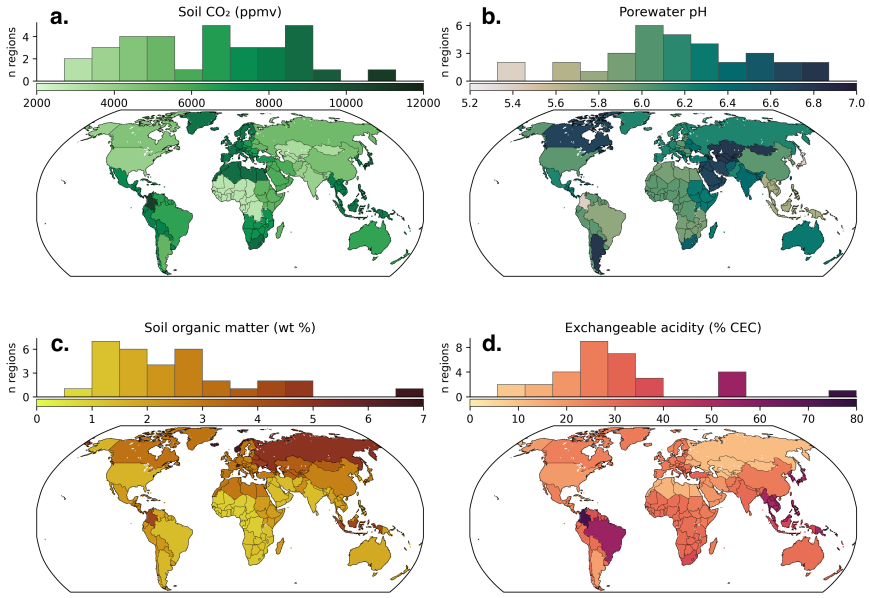


Figure S3: Spinup targets by GCAM region. (a) Soil CO_2; (b) Porewater pH; (c) Soil organic matter; (d) Exchangeable acidity. Each region gets the value of the representative cropland cell (see Methods). Each region's spinup simulation is iteratively tuned until these four targets are matched.

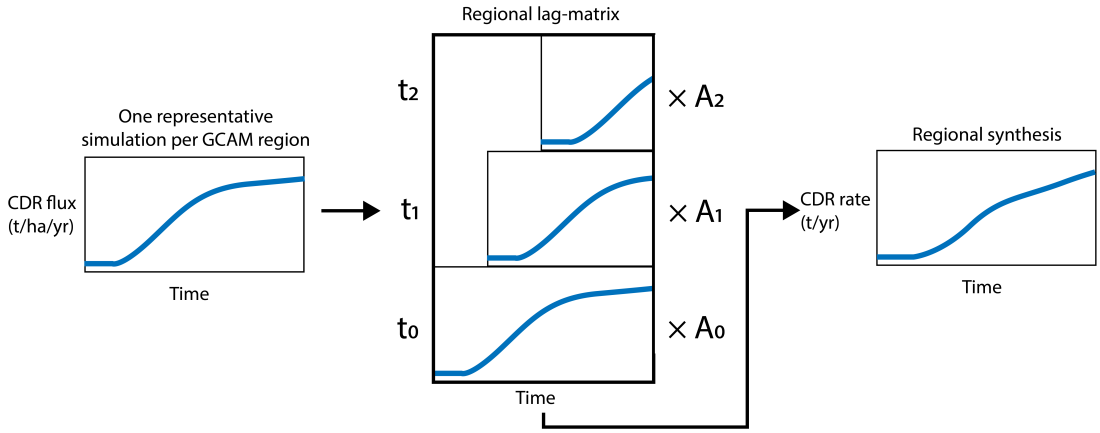


Figure S4: CDR fluxes are scaled to regional rates by determining the amount of cropland area required to accommodate a new application cohort when a region's total scale of rock spreading grows. We start with a single representative run (left panel) and restart that run every year, multiplying its fluxes by the land area of the new cohort. Finally, we sum all cohorts to get a single, regional CDR rate over time.

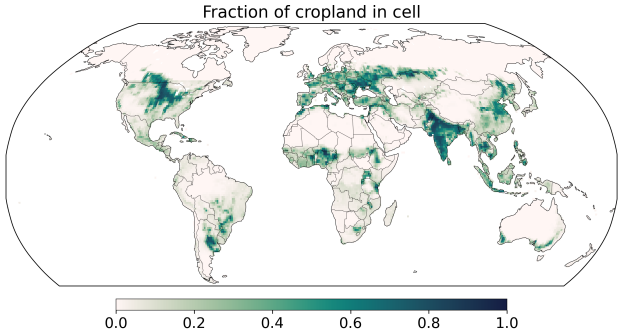


Figure S5: Fraction of cropland in each grid cell, using the data of Mehrabi et al. (2024).

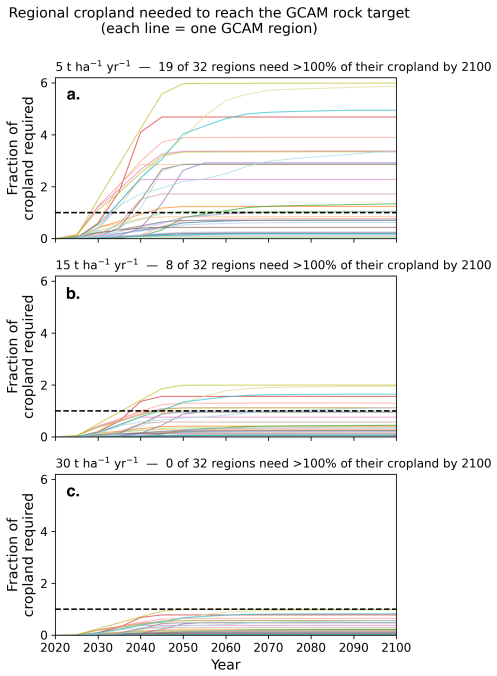


Figure S6: Fraction of regional cropland required to meet GCAM's target rock application at three different application fluxes. (a) 5 t ha^{-1} yr^{-1} of basalt; (b) 15 t ha^{-1} yr^{-1}; (c) 30 t ha^{-1} yr^{-1}.

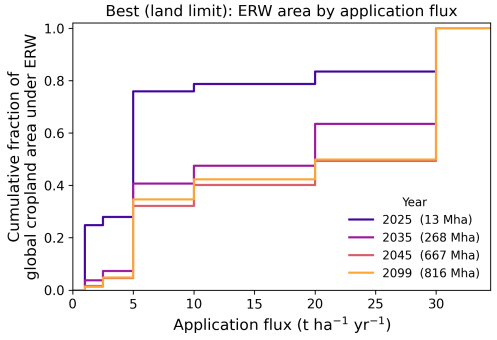


Figure S7: Cumulative distribution function of feedstock application flux by the fraction of global cropland area used for ERW. By 2045, about half of global croplands used for ERW are receiving at least 30 t ha^{-1} yr^{-1} of unweathered rock.

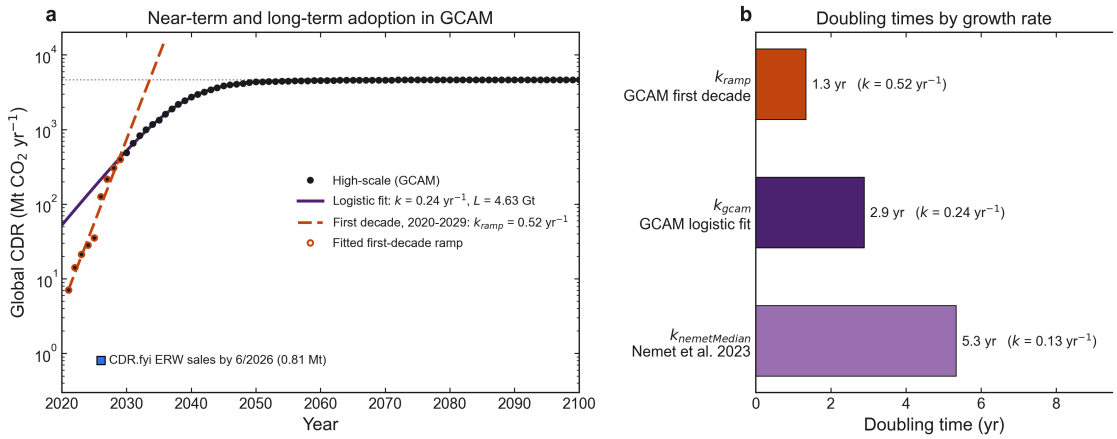


Figure S8: (a) GCAM's ERW adoption curve has two stages — a near-term stage of rapid growth in the first decade, and slower growth after that. By 2026, GCAM's estimated CDR is about 2 orders of magnitude above cumulative ERW sales. (b) Doubling times by logistic growth coefficient. The median logistic growth coefficient from Nemet et al. (2023) is about 0.13 per year, or a doubling time of 5.3 years.

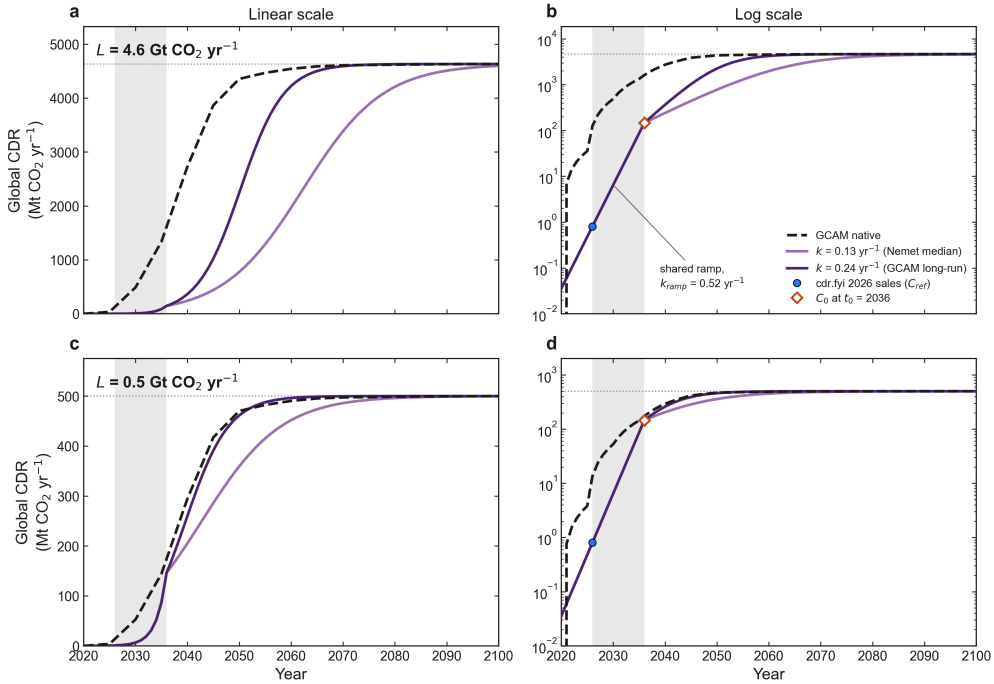


Figure S9: ERW adoption curves in linear (a, c) and log (b, d) scales to show detail. All curves share the same steep ramp in the first decade (2026–2036), and then evolve based on two different growth rate coefficients. The dark purple curve shows k=0.24 yr^{-1}, the best fit to the GCAM native curve, and the light purple line shows k=0.13 yr^{-1}, consistent with the median logistic coefficient of Nemet et al. (2023).

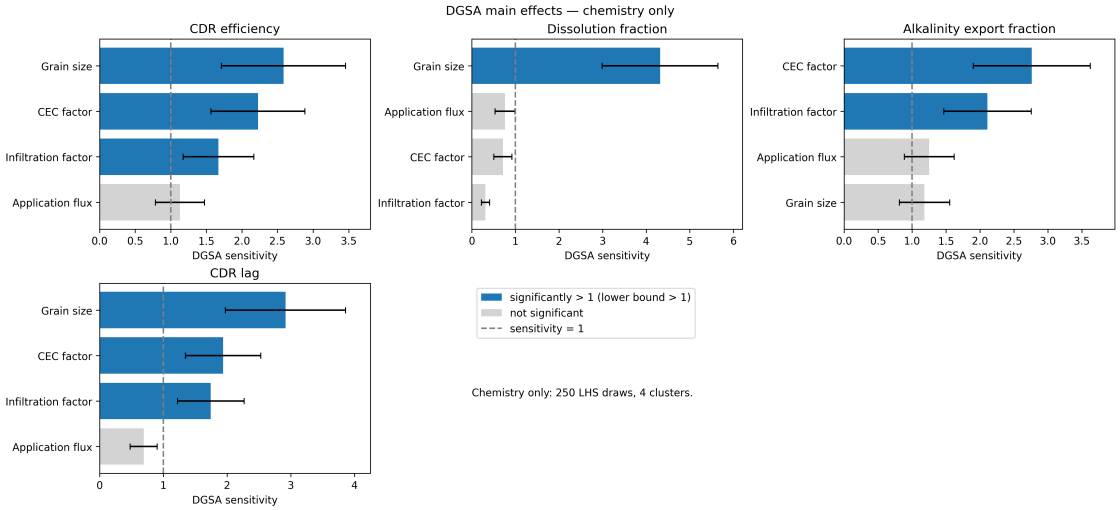


Figure S10: DGSA results for four response variables. CDR efficiency, dissolution fraction, and alkalinity export fraction terms are single-value, time-integrated. The lag between application and CDR reflects the time lag in years between when the rock is spread and when CDR in the form of alkalinity export occurs.

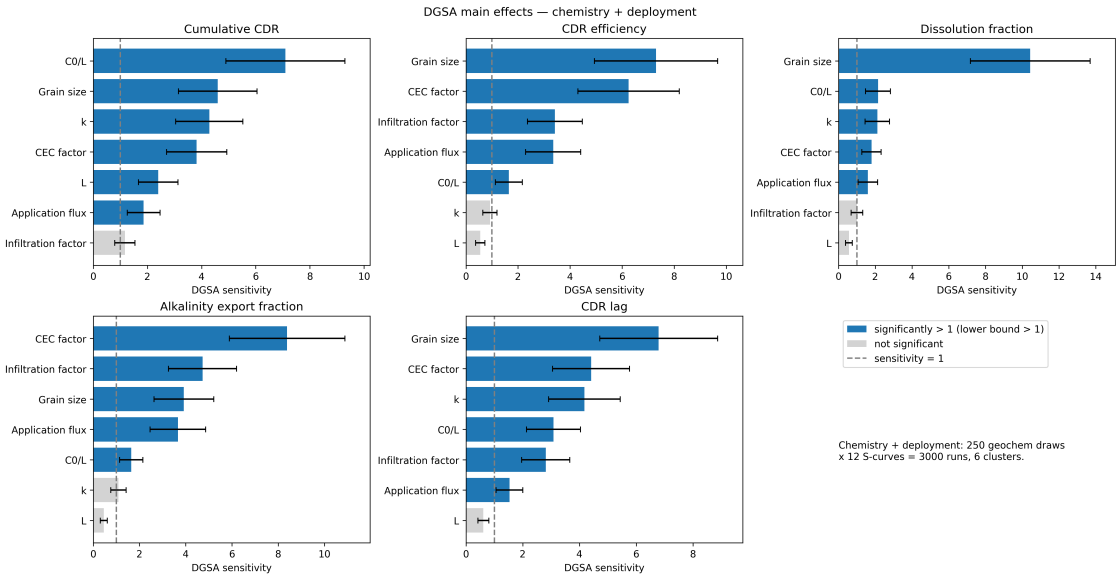


Figure S11: As in Figure S10, but with three additional input variables reflecting terms in the logistic growth curve for CDR adoption, and cumulative CDR as an additional response variable, defined over time. C_0/L refers to the gap between the reference CDR capacity, C_0, and the saturation capacity, L. k refers to the growth coefficient, which sets the amount of time it takes to reach L from C_0.

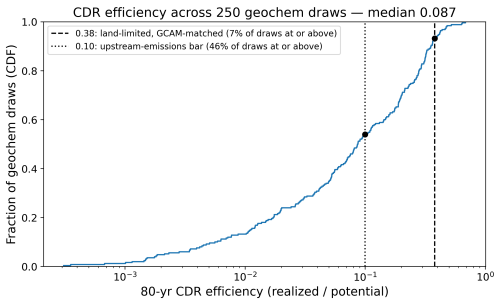


Figure S12: CDF of time-integrated CDR efficiency for the fixed schedule DGSA run. The simulation based on the GCAM case is more efficient than 93% of all Latin hypercube sampler draws. 54% of simulations have less than 10% efficiency — a rough threshold for the efficiency required to offset upstream emissions.

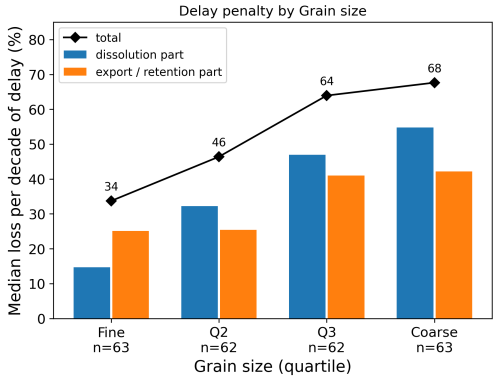


Figure S13: CDR efficiency loss per decade of delay in the temporal centroid of rock application in the DGSA multi-schedule runs. Efficiency loss is driven by lags in both dissolution and alkalinity export, both of which are amplified by coarser feedstock. Less initial specific surface area leads to slower dissolution and, consequently, slower neutralization of reserve acidity. If we assume a roughness factor of 10, the grain size quartiles correspond to radii of 3.3–9.7, 9.9–28, 29–84, and 85–250 μm, respectively.

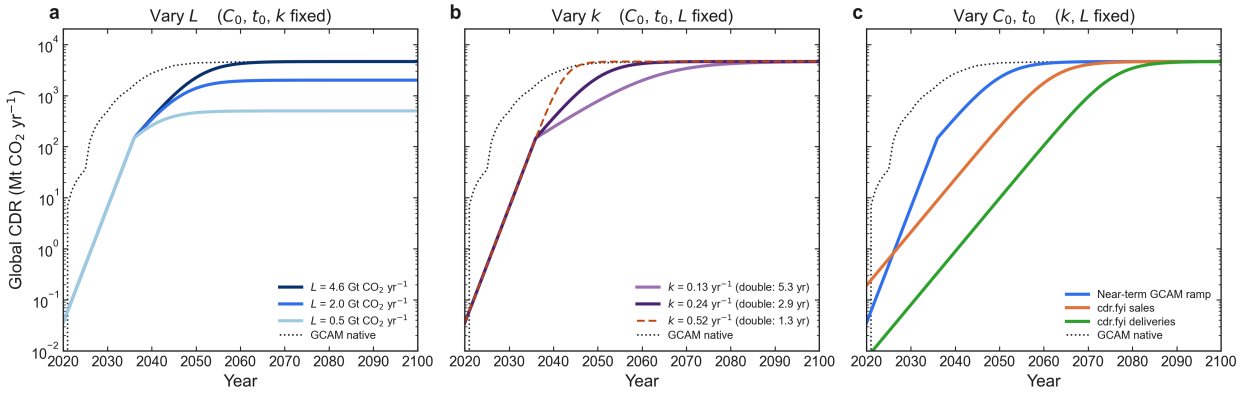


Figure S14: Adoption curve responses to varying terms in the logistic growth curve. (a) L sets the asymptote of the scale rate; (b) k sets the logistic growth coefficient; (c) the reference point is defined by a capacity, C_0, and time, t_0, around which the rest of the curve is built. Curves for cdr.fyi sales and deliveries refer to fixing the reference point at cumulative tonnes of EW CDR sold or delivered by 6/2026, according to cdr.fyi.

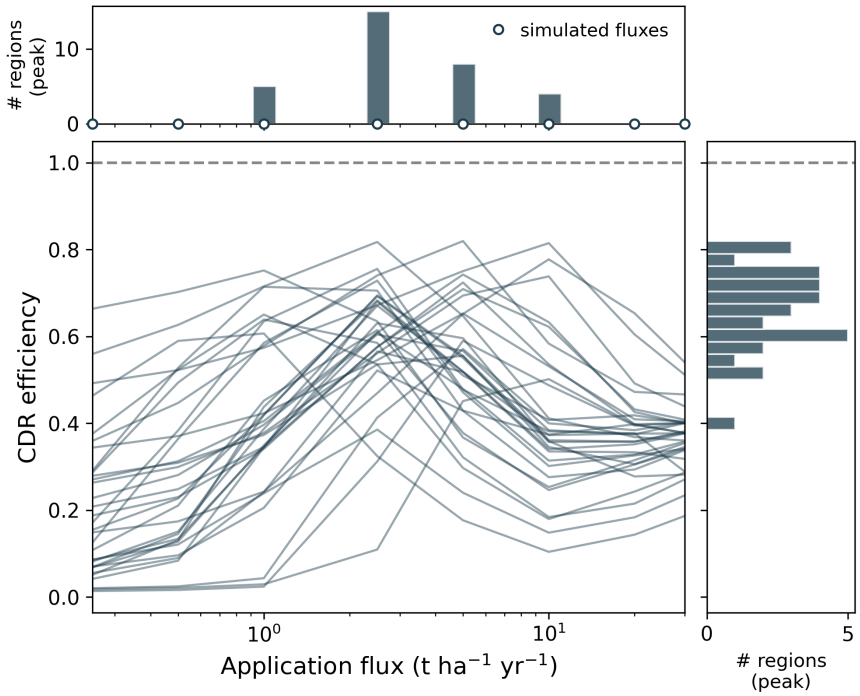


Figure S15: CDR efficiencies for each of GCAM's 32 geopolitical regions using the same grain size of Figure 1 from the main text. Histograms show the distribution of CDR efficiencies and the peak application fluxes. Note that CDR efficiency is strongly sensitive to the grain size (and initial specific surface area) of the feedstock, and these results use GCAM's fine-grained feedstock which leads to near-total dissolution.

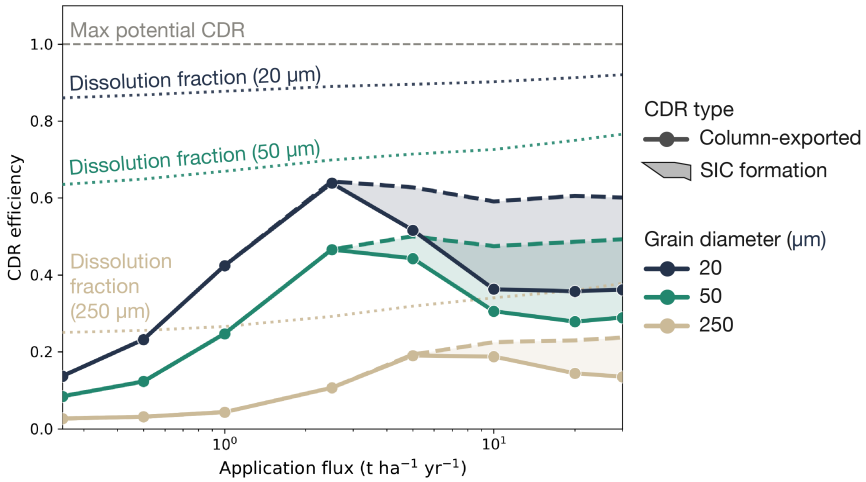


Figure S16: CDR efficiency by application flux for three different dust diameters (each with a roughness factor of 50). Coarser grains lower the total CDR efficiency largely by decreasing the dissolution efficiency. Coarser grains also shift the peak application flux to the right, as more rock is required to reach the alkalinity flux that drives calcite saturation.

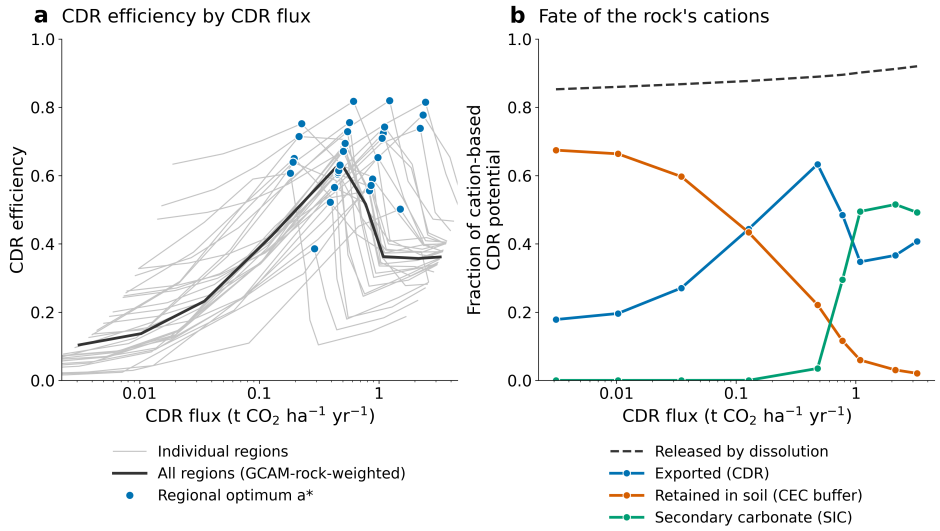


Figure S17: Time-mean CDR fluxes (a) by region (gray lines) and globally (black line); and (b) expressed as potential CDR based on cation sinks. Peaks in panel A reflect maximum CDR efficiency before or at the onset of secondary carbonate precipitation. CDR fluxes at those peaks span about 0.2–2 t/ha/yr.

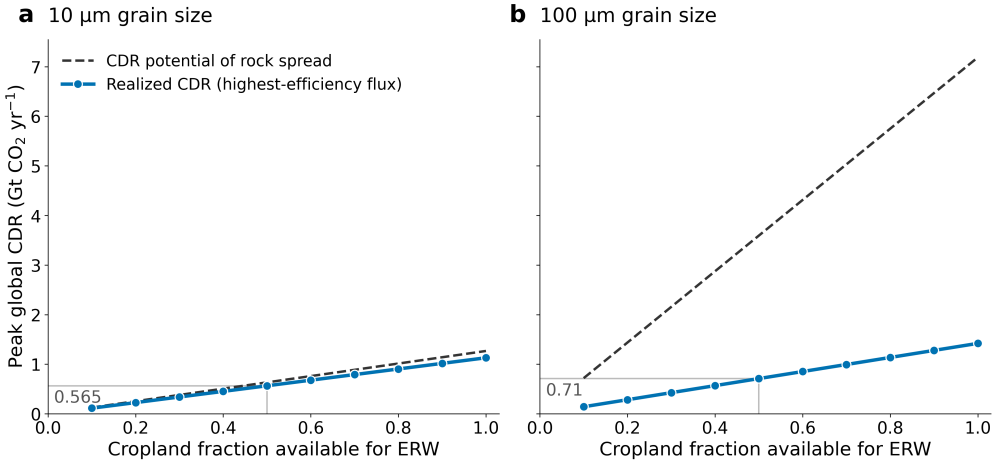


Figure S18: Peak global CDR rate assuming that every region spreads rock at the application flux that yields the highest CDR efficiency (therefore just before soil carbonate formation begins). Two grain sizes are shown: (a) 10 µm diameter and (b) 100 µm diameter. The 100 µm diameter feedstock achieves a higher maximum CDR rate but at much lower efficiency relative to the amount of rock spread.

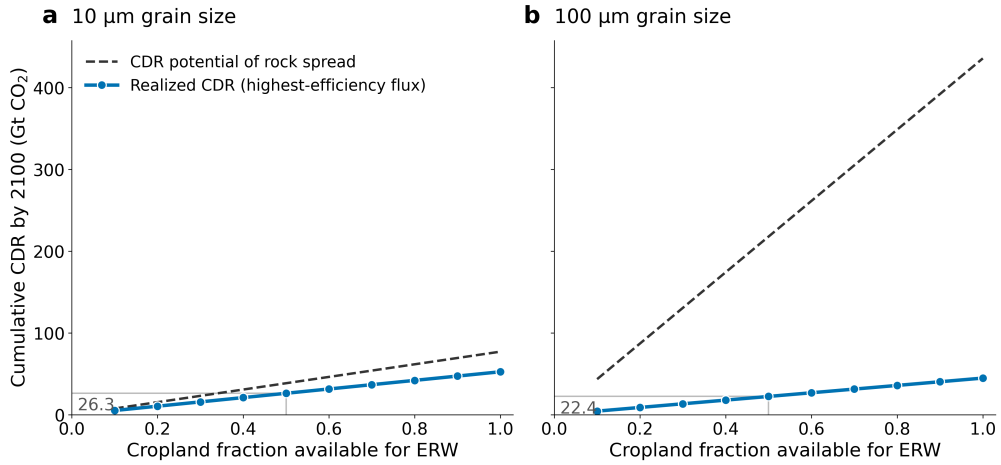


Figure S19: As in Figure S18, but for cumulative CDR by 2100.

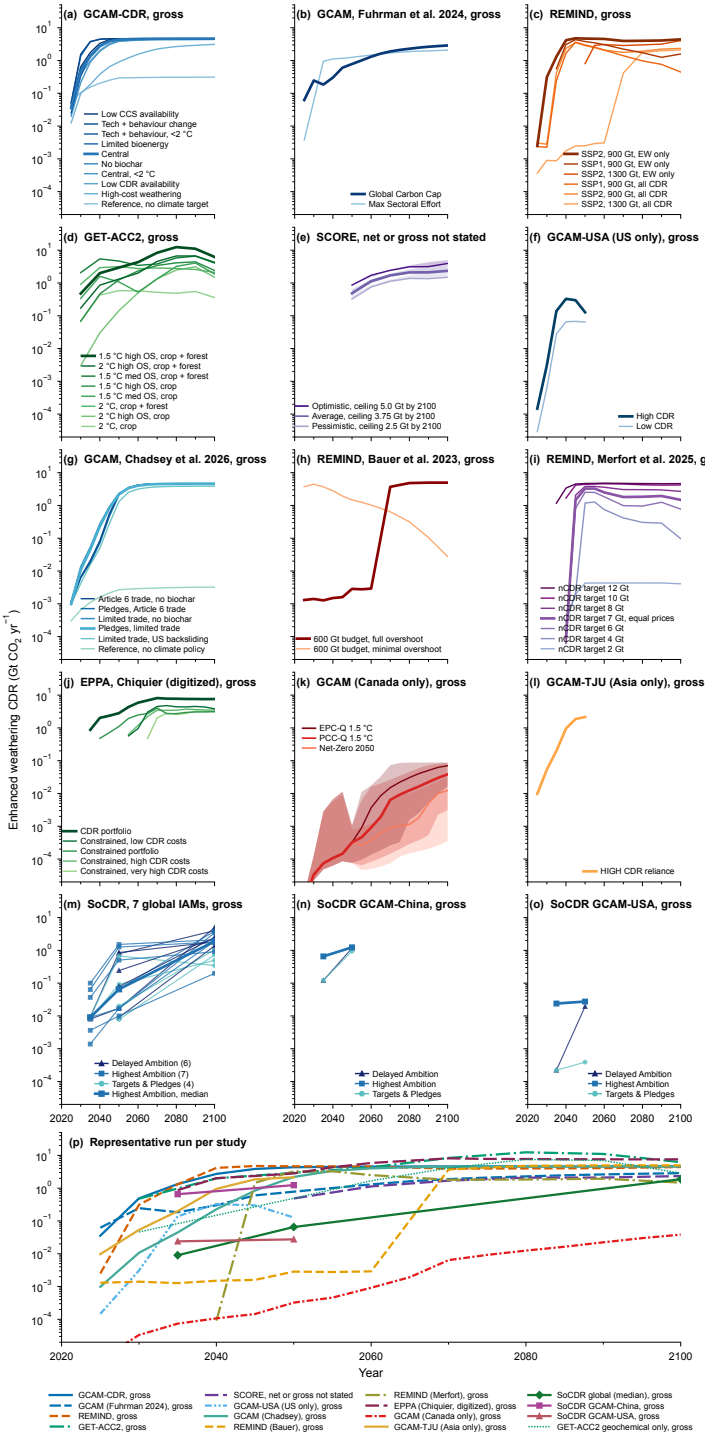


Figure S20: ERW CDR over time for each IAM study and the State of CDR report (Gidden et al., 2026), for every reported scenario. The bottom panel shows one representative run per study.

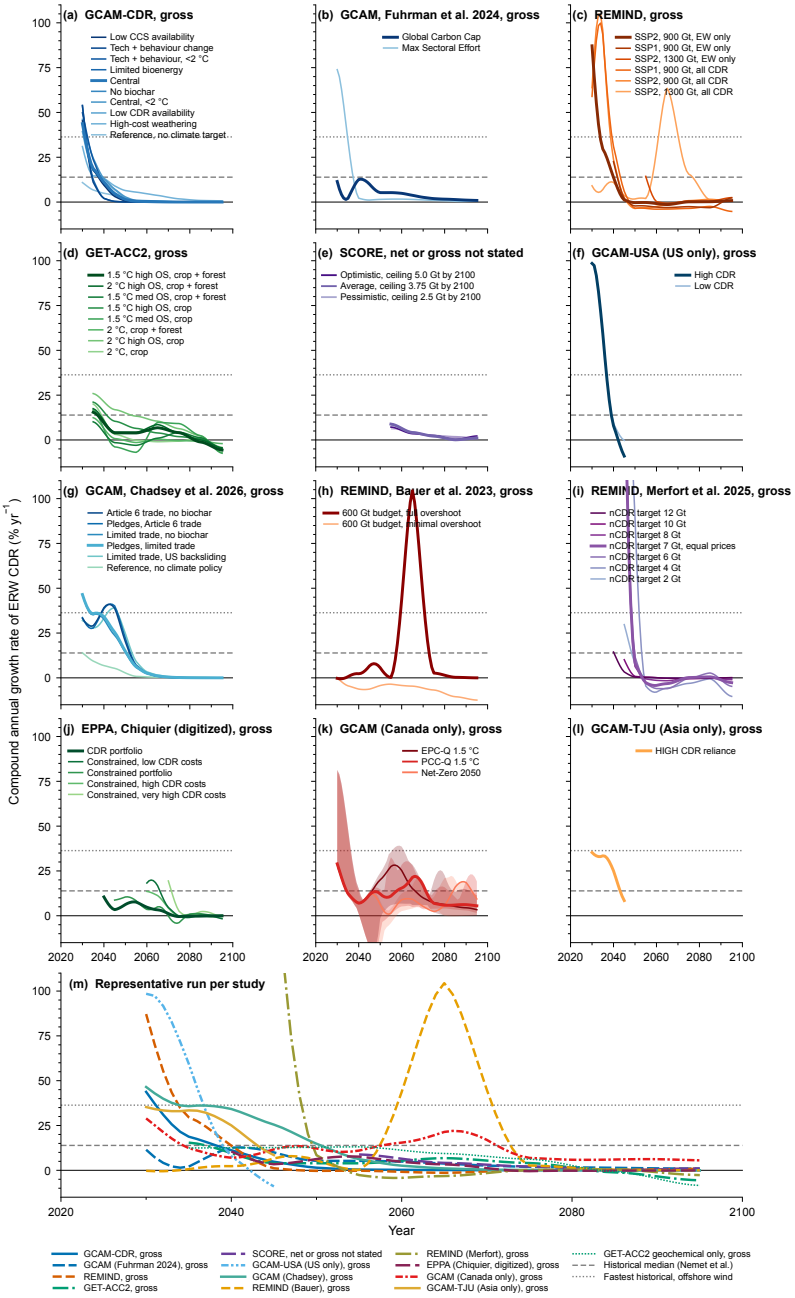


Figure S21: Compound annual growth rates over time for a series of regional and global scale ERW studies. Dotted and dashed lines show the compound annual growth rates equivalent to logistic coefficients of 0.31 yr^{-1} for offshore wind (36% yr^{-1}) and 0.13 yr^{-1}, the historical median (14% yr^{-1}) (Nemet et al., 2023). Growth rates decline toward zero as ERW adoption saturates.

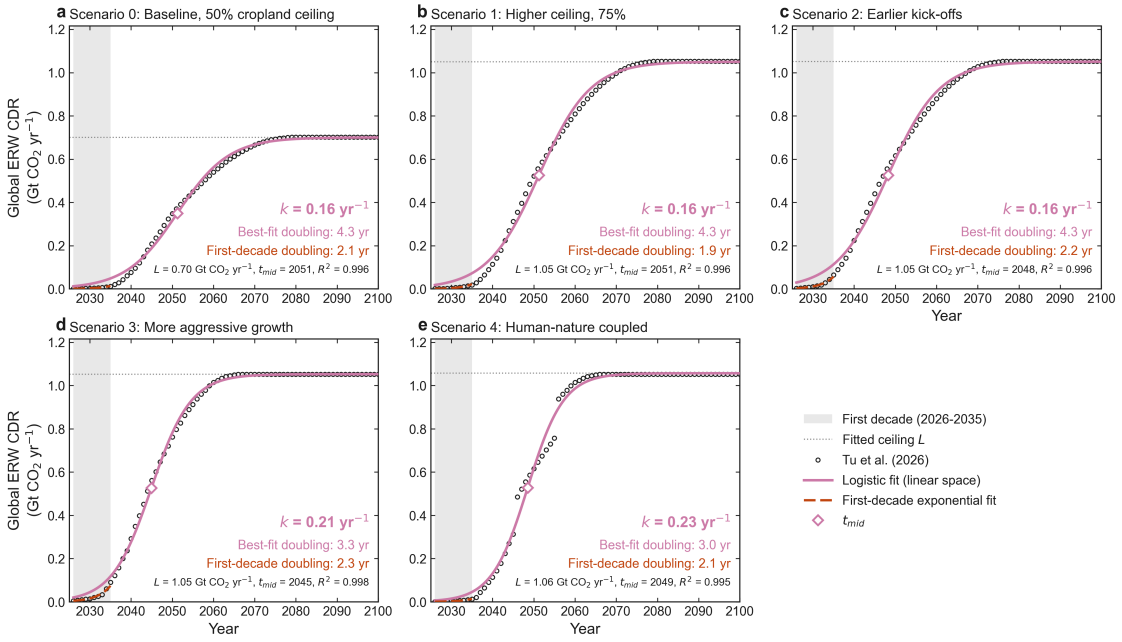


Figure S22: Best fit logistic curves for Tu et al. (2026) scenarios. Importantly, the technological diffusion model of Tu et al. (2026) does not require adoption to follow a logistic curve. We only show the best fits here to provide a direct comparison to the metrics we use to discuss adoption rates in GCAM. In both the GCAM simulations and the scenarios of Tu et al. (2026), near-term adoption is much faster than the best fit mid-term growth rate, so we report both the first decade and best fit doubling times for reference.

References

Ampah, J. D., Jin, C., Liu, H., Yao, M., Afrane, S., Adun, H., et al. (2024). Deployment expectations of multi-gigatonne scale carbon removal could have adverse impacts on Asia's energy-water-land nexus. *Nature Communications*, *15*(1), 6342. https://doi.org/10.1038/s41467-024-50594-5

Anand, S. K., Bertagni, M., Aburto, F., & Calabrese, S. (2026). Soil Structure and Mixing Controls on Water-Rock Contact: Implications for Enhanced Weathering. *Water Resources Research*, *62*(2), e2025WR041479. https://doi.org/10.1029/2025WR041479

Anderson, K., & Peters, G. (2016). The trouble with negative emissions. *Science*, *354*(6309), 182–183. https://doi.org/10.1126/science.aah4567

Aviso, K. B., Foo, D. C. Y., Gue, I. H. V., Migo-Sumagang, M. V., Tan, R. R., & Tan, Y. L. (2026). Indirect carbon emissions of enhanced weathering in Malaysia. *Carbon Footprints*, *5*(1). https://doi.org/10.20517/cf.2025.54

Baek, S. H., Kanzaki, Y., Lora, J. M., Planavsky, N., Reinhard, C. T., & Zhang, S. (2023). Impact of Climate on the Global Capacity for Enhanced Rock Weathering on Croplands. *Earth's Future*, *11*(8), e2023EF003698. https://doi.org/10.1029/2023EF003698

Batjes, N. H. (2016). Harmonized soil property values for broad-scale modelling (WISE30sec) with estimates of global soil carbon stocks. *Geoderma*, *269*, 61–68. https://doi.org/10.1016/j.geoderma.2016.01.034

Bauer, N., Keller, D. P., Garbe, J., Karstens, K., Piontek, F., Von Bloh, W., et al. (2023). Exploring risks and benefits of overshooting a 1.5 °C carbon budget over space and time. *Environmental Research Letters*, *18*(5), 054015. https://doi.org/10.1088/1748-9326/accd83

Beerling, D. J., Kantzas, E. P., Lomas, M. R., Wade, P., Eufrasio, R. M., Renforth, P., et al. (2020). Potential for large-scale CO2 removal via enhanced rock weathering with croplands. *Nature*, *583*(7815), 242–248. https://doi.org/10.1038/s41586-020-2448-9

Beerling, D. J., Epihov, D. Z., Kantola, I. B., Masters, M. D., Reershemius, T., Planavsky, N. J., et al. (2024). Enhanced weathering in the US Corn Belt delivers carbon removal with agronomic benefits. *Proceedings of the National Academy of Sciences*, *121*(9), e2319436121. https://doi.org/10.1073/pnas.2319436121

Beerling, D. J., Reinhard, C. T., James, R. H., Khan, A., Pidgeon, N., & Planavsky, N. J. (2025). Challenges and opportunities in scaling enhanced weathering for carbon dioxide removal. *Nature Reviews Earth & Environment*. https://doi.org/10.1038/s43017-025-00713-7

Bindl, M., Edwards, M. R., & Cui, R. Y. (2025). Risks of relying on uncertain carbon dioxide removal in climate policy. *Nature Communications*, *16*(1), 5958. https://doi.org/10.1038/s41467-025-61106-4

Buckingham, F. L., Henderson, G. M., Holdship, P., & Renforth, P. (2022). Soil core study indicates limited CO2 removal by enhanced weathering in dry croplands in the UK. *Applied Geochemistry*, *147*, 105482. https://doi.org/10.1016/j.apgeochem.2022.105482

Buma, B., Dietzen, C., Gordon, D. R., Maher, K., Neumann, R. B., Planavsky, N. J., et al. (2026). Expert elicitation on agricultural enhanced weathering reveals carbon dioxide removal potential and uncertainties in loss pathways. *Communications Earth & Environment*, *7*(1), 376. https://doi.org/10.1038/s43247-026-03375-5

CDR.fyi. (2026). Carbon Removal Leaderboards. Retrieved from https://www.cdr.fyi

Chadsey, R., Harris, C., Diaoglou, V., Pratama, Y., Lamb, W. F., Rhalem, O., et al. (2026). Carbon dioxide removal consistent with climate pledges: A multi-model assessment of regional potential. *Environmental Science: Advances*. https://doi.org/10.1039/D6VA00109B

Chambers, B. J., & Garwood, T. W. D. (1998). Lime loss rates from arable and grassland soils. *The Journal of Agricultural Science*, *131*(4), 455–464. https://doi.org/10.1017/S0021859698005954

Chiquier, S., Fajardy, M., & Mac Dowell, N. (2022). CO_2 removal and 1.5 °C: What, when, where, and how? *Energy Advances*, *1*(8), 524–561. https://doi.org/10.1039/D2YA00108J

Chiquier, S., Gurgel, A., Morris, J., Chen, Y.-H. H., & Paltsev, S. (2025). Integrated assessment of carbon dioxide removal portfolios: Land, energy, and economic trade-offs for climate policy. *Environmental Research Letters*, *20*(2), 024002. https://doi.org/10.1088/1748-9326/ada4c0

Cifu, M., Xiaonan, L., Zhihong, C., Zhengyi, H., & Wanzhu, M. (2004). Long-term effects of lime application on soil acidity and crop yields on a red soil in Central Zhejiang. *Plant and Soil*, *265*(1-2), 101–109. https://doi.org/10.1007/s11104-005-8941-y

Clow, D. W., & Mast, M. A. (2010). Mechanisms for chemostatic behavior in catchments: Implications for CO2 consumption by mineral weathering. *Chemical Geology*, *269*(1-2), 40–51. https://doi.org/10.1016/j.chemgeo.2009.09.014

Cobo, S., & Guillén-Gosálbez, G. (2026). Delayed Climate Benefits and Toxicity Risks Could Hinder the Sustainable Deployment of Enhanced Weathering. *Environmental Science & Technology*, *60*(35), 24676–24686. https://doi.org/10.1021/acs.est.6c08993

Deprez, A., Leadley, P., Dooley, K., Williamson, P., Cramer, W., Gattuso, J.-P., et al. (2024). Sustainability limits needed for CO_2 removal. *Science*, *383*(6682), 484–486. https://doi.org/10.1126/science.adj6171

Derry, L. A., Maher, K., & Chadwick, O. A. (2026). Critical zone processes limit alkalinity export from natural basaltic systems. *Nature*. https://doi.org/10.1038/s41586-026-10936-3

Dietzen, C., & Rosing, M. T. (2023). Quantification of CO2 uptake by enhanced weathering of silicate minerals applied to acidic soils. *International Journal of Greenhouse Gas Control*, *125*, 103872. https:

//doi.org/10.1016/j.ijggc.2023.103872

Eufrasio, R. M., Kantzas, E. P., Edwards, N. R., Holden, P. B., Pollitt, H., Mercure, J.-F., et al. (2022). Environmental and health impacts of atmospheric CO2 removal by enhanced rock weathering depend on nations' energy mix. *Communications Earth & Environment*, *3*(1), 106. https://doi.org/10.1038/s43247-022-00436-3

Fageria, N. K., & Baligar, V. C. (2008). Chapter 7 Ameliorating Soil Acidity of Tropical Oxisols by Liming For Sustainable Crop Production. In *Advances in Agronomy* (Vol. 99, pp. 345–399). Elsevier. https://doi.org/10.1016/S0065-2113(08)00407-0

Fenwick, D., Scheidt, C., & Caers, J. (2014). Quantifying Asymmetric Parameter Interactions in Sensitivity Analysis: Application to Reservoir Modeling. *Mathematical Geosciences*, *46*(4), 493–511. https://doi.org/10.1007/s11004-014-9530-5

Fuhrman, J., Bergero, C., Weber, M., Monteith, S., Wang, F. M., Clarens, A. F., et al. (2023). Diverse carbon dioxide removal approaches could reduce impacts on the energy–water–land system. *Nature Climate Change*, *13*(4), 341–350. https://doi.org/10.1038/s41558-023-01604-9

Fuhrman, J., Speizer, S., O'Rourke, P., Peters, G. P., McJeon, H., Monteith, S., et al. (2024). Ambitious efforts on residual emissions can reduce CO_2 removal and lower peak temperatures in a net-zero future. *Environmental Research Letters*, *19*(6), 064012. https://doi.org/10.1088/1748-9326/ad456d

Gaillardet, J., Calmels, D., Romero-Mujalli, G., Zakharova, E., & Hartmann, J. (2019). Global climate control on carbonate weathering intensity. *Chemical Geology*, *527*, 118762. https://doi.org/10.1016/j.chemgeo.2018.05.009

Gaucher, Y., Tanaka, K., Johansson, D. J. A., Goll, D. S., & Ciais, P. (2025). Leveraging ecosystems responses to enhanced rock weathering in mitigation scenarios. *Nature Communications*, *16*(1), 3021. https://doi.org/10.1038/s41467-025-58284-6

Gidden, M. J., Portugal-Pereira, J., Apeaning, R., Bergero, C., Daioglou, V., Drouet, L., et al. (2026). Chapter 8: Paris-consistent CDR scenarios. In M. R. Edwards (Ed.), *The State of Carbon Dioxide Removal* (3rd ed.). Retrieved from https://www.stateofcdr.org/report/3rd-edition

Goddéris, Y., Williams, J. Z., Schott, J., Pollard, D., & Brantley, S. L. (2010). Time evolution of the mineralogical composition of Mississippi Valley loess over the last 10kyr: Climate and geochemical modeling. *Geochimica Et Cosmochimica Acta*, *74*(22), 6357–6374. https://doi.org/10.1016/j.gca.2010.08.023

Goulding, K. W. T. (2016). Soil acidification and the importance of liming agricultural soils with particular reference to the United Kingdom. *Soil Use and Management*, *32*(3), 390–399. https://doi.org/10.1111/sum.12270

Guo, J. H., Liu, X. J., Zhang, Y., Shen, J. L., Han, W. X., Zhang, W. F., et al. (2010). Significant Acidification in

Major Chinese Croplands. *Science*, *327*(5968), 1008–1010. https://doi.org/10.1126/science.1182570

Gwiazda, R. H., & Broecker, W. S. (1994). The separate and combined effects of temperature, soil pCO_2, and organic acidity on silicate weathering in the soil environment: Formulation of a model and results. *Global Biogeochemical Cycles*, *8*(2), 141–155. https://doi.org/10.1029/94GB00491

Hammes, J. S., Hartmann, J., Barth, J. A. C., Linke, T., Smet, I., Hagens, M., et al. (2025, November). Soil processes govern alkalinity and cation retention in enhanced weathering for carbon dioxide removal. Biogeochemistry: Land. https://doi.org/10.5194/egusphere-2025-5402

Harris, C., Daioglou, V., Tagomori, I., Rhalem, O., Doelman, J., Fuhrman, J., et al. (2026, June). Carbon Dioxide Removal Supply Curves: A Multi-Model Assessment. EarthArXiv. https://doi.org/10.31223/X5C19K

Hasemer, H., Borevitz, J., & Buss, W. (2024). Measuring enhanced weathering: Inorganic carbon-based approaches may be required to complement cation-based approaches. *Frontiers in Climate*, *6*, 1352825. https://doi.org/10.3389/fclim.2024.1352825

Haynes, R. J. (1984). Lime and Phosphate in the Soil-Plant System. In *Advances in Agronomy* (Vol. 37, pp. 249–315). Elsevier. https://doi.org/10.1016/S0065-2113(08)60456-3

Helyar, K., Cregan, P., & Godyn, D. (1990). Soil acidity in New-South-Wales - Current pH values and estimates of acidification rates. *Australian Journal of Soil Research*, *28*(4), 523–537. https://doi.org/10.1071/SR9900523

Hersbach, H., Bell, B., Berrisford, P., Hirahara, S., Horányi, A., Muñoz-Sabater, J., et al. (2020). The ERA5 global reanalysis. *Quarterly Journal of the Royal Meteorological Society*, *146*(730), 1999–2049. https://doi.org/10.1002/qj.3803

Hersbach, H., Bell, B., Berrisford, P., Biavati, G., Horányi, A., Muñoz Sabater, J., et al. (2023). ERA5 hourly data on single levels from 1940 to present. Copernicus Climate Change Service (C3S) Climate Data Store (CDS). https://doi.org/10.24381/cds.adbb2d47

Holden, F. J., Davies, K., Bird, M. I., Hume, R., Green, H., Beerling, D. J., & Nelson, P. N. (2024). In-field carbon dioxide removal via weathering of crushed basalt applied to acidic tropical agricultural soil. *Science of The Total Environment*, *955*, 176568. https://doi.org/10.1016/j.scitotenv.2024.176568

Holz, C., Siegel, L. S., Johnston, E., Jones, A. P., & Sterman, J. (2018). Ratcheting ambition to limit warming to 1.5 °C – trade-offs between emission reductions and carbon dioxide removal. *Environmental Research Letters*, *13*(6), 064028. https://doi.org/10.1088/1748-9326/aac0c1

Javadi, P., O'Rourke, P., Fuhrman, J., Loughlin, D. H., Doney, S. C., Shobe, W., et al. (2026). Large-Scale Carbon Removal Will Create Public Health, Economic, and Climate Trade-Offs. *Environmental Science & Technology*, *60*(24), 17192–17205. https://doi.org/10.1021/acs.est.5c17950

Jessen, S., Jakobsen, R., Looms, M., Ambus, P., & Postma, D. (2026). Subsoil acidity causes long delays in

644 inorganic carbon sequestration by Enhanced Weathering. arXiv. https://doi.org/10.48550/arXiv.2607.
645 01835
646 Kanzaki, Y., & Reinhard, C. (2025). SCEPTER v1.0.2. Zenodo. https://doi.org/10.5281/zenodo.16885370
647 Kanzaki, Y., Zhang, S., Planavsky, N. J., & Reinhard, C. T. (2022). Soil Cycles of Elements simulator for Pre-
648 dicting TERrestrial regulation of greenhouse gases: SCEPTER v0.9. *Geoscientific Model Development*,
649 *15*(12), 4959–4990. https://doi.org/10.5194/gmd-15-4959-2022
650 Kanzaki, Y., Planavsky, N. J., & Reinhard, C. T. (2023). New estimates of the storage permanence and
651 ocean co-benefits of enhanced rock weathering. *PNAS Nexus*, *2*(4), pgad059. https://doi.org/10.
652 1093/pnasnexus/pgad059
653 Kanzaki, Y., Chiaravalloti, I., Zhang, S., Planavsky, N. J., & Reinhard, C. T. (2024). In silico calculation of soil pH
654 by SCEPTER v1.0. *Geoscientific Model Development*, *17*(10), 4515–4532. https://doi.org/10.5194/gmd-
655 17-4515-2024
656 Kanzaki, Y., Planavsky, N. J., Zhang, S., Jordan, J., Suhrhoff, T. J., & Reinhard, C. T. (2025). Soil cation
657 storage is a key control on the carbon removal dynamics of enhanced weathering. *Environmental*
658 *Research Letters*, *20*(7), 074055. https://doi.org/10.1088/1748-9326/ade0d5
659 Kukla, T. (2026a). iam-rtm-compare: Analysis code for “Integrated assessment models overestimate
660 carbon removal from enhanced weathering.” GitHub. Retrieved from https://github.com/carbonplan/
661 iam-rtm-compare
662 Kukla, T. (2026b). SCEPTER v1.0.2 with CarbonPlan Modifications. GitHub. Retrieved from https://github.
663 com/carbonplan/SCEPTER
664 Kukla, T. (2026c, November). Data for reactive transport simulations of enhanced weathering to replicate
665 integrated assessment model deployment. Zenodo. https://doi.org/10.5281/zenodo.24206818
666 Kukla, T. (2026d, November). Enhanced weathering scoping model synthesis. Zenodo. https://doi.org/10.
667 5281/zenodo.24387133
668 Larkin, C. S., Andrews, M. G., Pearce, C. R., Yeong, K. L., Beerling, D. J., Bellamy, J., et al. (2022). Quantifica-
669 tion of CO2 removal in a large-scale enhanced weathering field trial on an oil palm plantation in Sabah,
670 Malaysia. *Frontiers in Climate*, *4*, 959229. https://doi.org/10.3389/fclim.2022.959229
671 Levy, C. R., Almaraz, M., Beerling, D. J., Raymond, P., Reinhard, C. T., Suhrhoff, T. J., & Taylor, L. (2024).
672 Enhanced Rock Weathering for Carbon Removal–Monitoring and Mitigating Potential Environmental
673 Impacts on Agricultural Land. *Environmental Science & Technology*, *58*(39), 17215–17226. https:
674 //doi.org/10.1021/acs.est.4c02368
675 Li, Z., Planavsky, N. J., & Reinhard, C. T. (2024). Geospatial assessment of the cost and energy demand
676 of feedstock grinding for enhanced rock weathering in the coterminous United States. *Frontiers in*

Climate, *6*, 1380651. https://doi.org/10.3389/fclim.2024.1380651

Long, R. P., Bailey, S. W., Horsley, S. B., Hall, T. J., Swistock, B. R., & DeWalle, D. R. (2015). Long-Term Effects of Forest Liming on Soil, Soil Leachate, and Foliage Chemistry in Northern Pennsylvania. *Soil Science Society of America Journal*, *79*(4), 1223–1236. https://doi.org/10.2136/sssaj2014.11.0465

Maher, K., Rogers, B., Perzan, Z., & Kukla, T. (2026). Surface Proton Reservoirs Constrain Alkalinity Export from Enhanced Weathering. *Environmental Science & Technology*. https://doi.org/10.1021/acs.est.6c03236

Maxbauer, D. P., Milliken, E., Yambing, J. R., Watson, E., Gregg, R. B., Swanson, L., et al. (2026). Evidence for carbon dioxide removal via enhanced rock weathering with steel slag, though not basalt, in a midwestern U.S. Field trial. *Frontiers in Climate*, *7*, 1657058. https://doi.org/10.3389/fclim.2025.1657058

Mayer, K. U., Bea, S. A., Su, D., Soong, J., Mills, J., & Benner, S. G. (2025, December). Carrying capacity as constraint for maximum efficient CDR in agricultural soils. In Review. https://doi.org/10.21203/rs.3.rs-7811095/v1

Mehrabi, Z., Tong, K., Fortin, J., Stanimirova, R., Friedl, M., & Ramankutty, N. (2024, August). Global agricultural lands in the year 2015. ESSD – Land/Land Cover and Land Use. https://doi.org/10.5194/essd-2024-279

Merfort, A., Strefler, J., Abrahão, G., Bauer, N., Dorndorf, T., Kriegler, E., et al. (2025). Separating CO2 emission from removal targets comes with limited cost impacts. *Nature Communications*, *16*(1), 5298. https://doi.org/10.1038/s41467-025-60606-7

Moosdorf, N., Renforth, P., & Hartmann, J. (2014). Carbon Dioxide Efficiency of Terrestrial Enhanced Weathering. *Environmental Science & Technology*, *48*(9), 4809–4816. https://doi.org/10.1021/es4052022

Morrow, D. R., Apeaning, R., & Guard, G. (2023). GCAM-CDR v1.0: Enhancing the representation of carbon dioxide removal technologies and policies in an integrated assessment model. *Geoscientific Model Development*, *16*(3), 1105–1118. https://doi.org/10.5194/gmd-16-1105-2023

Motlaghzadeh, K., Craik, N., Moreno-Cruz, J., Schweizer, V., Fuhrman, J., & Hipel, K. W. (2025). Applying equity principles leads to higher carbon removal obligations in Canada. *Communications Earth & Environment*, *6*(1), 88. https://doi.org/10.1038/s43247-025-02080-z

Nelson, P. N., & Su, N. (2010). Soil pH buffering capacity: A descriptive function and its application to some acidic tropical soils. *Soil Research*, *48*(3), 201–207. https://doi.org/10.1071/SR09150

Nemet, G., Greene, J., Müller-Hansen, F., & Minx, J. C. (2023). Dataset on the adoption of historical technologies informs the scale-up of emerging carbon dioxide removal measures. *Communications Earth & Environment*, *4*(1), 397. https://doi.org/10.1038/s43247-023-01056-1

Park, J., Yang, G., Satija, A., Scheidt, C., & Caers, J. (2016). DGSA: A Matlab toolbox for distance-based generalized sensitivity analysis of geoscientific computer experiments. *Computers & Geosciences*, *97*, 15–29. https://doi.org/10.1016/j.cageo.2016.08.021

Parker, M. B., & Walker, M. E. (1986). Soil pH and Manganese Effects on Manganese Nutrition of Peanut. *Agronomy Journal*, *78*(4), 614–620. https://doi.org/10.2134/agronj1986.00021962007800040011x

Perzan, Z. (2026, February). Zperzan/pyDGSA: V1.1.1. Zenodo. https://doi.org/10.5281/zenodo.18518681

Perzan, Z., & Maher, K. (2024). Transport, dispersion, and degradation of nonpoint source contaminants during flood-managed aquifer recharge. *Vadose Zone Journal*, *23*(2), e20307. https://doi.org/10.1002/vzj2.20307

Perzan, Z., Babey, T., Caers, J., Bargar, J. R., & Maher, K. (2021). Local and Global Sensitivity Analysis of a Reactive Transport Model Simulating Floodplain Redox Cycling. *Water Resources Research*, *57*(12), e2021WR029723. https://doi.org/10.1029/2021WR029723

Poggio, L., de Sousa, L. M., Batjes, N. H., Heuvelink, G. B. M., Kempen, B., Ribeiro, E., & Rossiter, D. (2021). SoilGrids 2.0: Producing soil information for the globe with quantified spatial uncertainty. *SOIL*, *7*(1), 217–240. https://doi.org/10.5194/soil-7-217-2021

Reershemius, T., Kelland, M. E., Jordan, J. S., Davis, I. R., D'Ascanio, R., Kalderon-Asael, B., et al. (2023). Initial Validation of a Soil-Based Mass-Balance Approach for Empirical Monitoring of Enhanced Rock Weathering Rates. *Environmental Science & Technology*, acs.est.3c03609. https://doi.org/10.1021/acs.est.3c03609

Renforth, P., & Henderson, G. (2017). Assessing ocean alkalinity for carbon sequestration: Ocean Alkalinity for C Sequestration. *Reviews of Geophysics*, *55*(3), 636–674. https://doi.org/10.1002/2016RG000533

Renforth, P., Pogge Von Strandmann, P. A. E., & Henderson, G. M. (2015). The dissolution of olivine added to soil: Implications for enhanced weathering. *Applied Geochemistry*, *61*, 109–118. https://doi.org/10.1016/j.apgeochem.2015.05.016

Rinder, T., & Von Hagke, C. (2021). The influence of particle size on the potential of enhanced basalt weathering for carbon dioxide removal – Insights from a regional assessment. *Journal of Cleaner Production*, *315*, 128178. https://doi.org/10.1016/j.jclepro.2021.128178

Rogers, B., & Maher, K. (2026). A thermodynamic framework for lime requirement and alkalinity production in acidic soils. *Geoderma*, *473*, 117956. https://doi.org/10.1016/j.geoderma.2026.117956

Schaber, T., Ekholm, T., Merikanto, J., & Partanen, A.-I. (2024). Prudent carbon dioxide removal strategies hedge against high climate sensitivity. *Communications Earth & Environment*, *5*(1), 285. https://doi.org/10.1038/s43247-024-01456-x

Shindell, D., & Rogelj, J. (2025). Preserving carbon dioxide removal to serve critical needs. *Nature Climate*

Change, *15*(4), 452–457. https://doi.org/10.1038/s41558-025-02251-y

Smith, P., Davis, S. J., Creutzig, F., Fuss, S., Minx, J., Gabrielle, B., et al. (2016). Biophysical and economic limits to negative CO2 emissions. *Nature Climate Change*, *6*(1), 42–50. https://doi.org/10.1038/nclimate2870

Steinwidder, L., Boito, L., Frings, P. J., Niron, H., Rijnders, J., De Schutter, A., et al. (2025). Beyond Inorganic C: Soil Organic C as a Key Pathway for Carbon Sequestration in Enhanced Weathering. *Global Change Biology*, *31*(7). https://doi.org/10.1111/gcb.70340

Strefler, J., Amann, T., Bauer, N., Kriegler, E., & Hartmann, J. (2018). Potential and costs of carbon dioxide removal by enhanced weathering of rocks. *Environmental Research Letters*, *13*(3), 034010. https://doi.org/10.1088/1748-9326/aaa9c4

Strefler, J., Bauer, N., Humpenöder, F., Klein, D., Popp, A., & Kriegler, E. (2021). Carbon dioxide removal technologies are not born equal. *Environmental Research Letters*, *16*(7), 074021. https://doi.org/10.1088/1748-9326/ac0a11

Su, C., Kang, R., Driscoll, C. T., Zhu, W., Goll, D. S., Huang, W., et al. (2026). Overlooked Soil Acidity Leads to Significant Overestimation of Carbon Sequestration in Enhanced Rock Weathering. *Environmental Science & Technology*, *60*(32), 22505–22516. https://doi.org/10.1021/acs.est.6c05139

Suhrhoff, T. J., Reinhard, C. T., Kanzaki, Y., Tsao, S. S.-E., Woollen, B., Reershemius, T., et al. (2026). Agricultural liming is a carbon sink in the Mississippi River Basin. *Nature*, *658*(8134), 113–118. https://doi.org/10.1038/s41586-026-11040-2

Suhrhoff, T. J., Dietzen, C., Kukla, T., Lunstrum, A., Reershemius, T., Thompson, J., et al. (2026, July). An Ecosystem of Carbon Dioxide Removal Reviews – Part 3: Enhanced Weathering. CDRXIV. https://doi.org/10.70212/cdrxiv.2026417.v1

Taylor, L. L., Driscoll, C. T., Groffman, P. M., Rau, G. H., Blum, J. D., & Beerling, D. J. (2021). Increased carbon capture by a silicate-treated forested watershed affected by acid deposition. *Biogeosciences*, *18*(1), 169–188. https://doi.org/10.5194/bg-18-169-2021

Te Pas, E. E. E. M., Chang, E., Marklein, A. R., Comans, R. N. J., & Hagens, M. (2025). Accounting for retarded weathering products in comparing methods for quantifying carbon dioxide removal in a short-term enhanced weathering study. *Frontiers in Climate*, *6*, 1524998. https://doi.org/10.3389/fclim.2024.1524998

Tu, Y., Rafols, R., Xu, Y., Butler, N., Ababneh, L., Tao, F., et al. (2026). Scaling up enhanced rock weathering for equitable climate change mitigation. *Communications Sustainability*, *1*(1), 32. https://doi.org/10.1038/s44458-026-00034-w

Vienne, A., Frings, P., Poblador, S., Steinwidder, L., Rijnders, J., Schoelynck, J., et al. (2024). Earthworms in

an enhanced weathering mesocosm experiment: Effects on soil carbon sequestration, base cation exchange and soil CO2 efflux. *Soil Biology and Biochemistry*, *199*, 109596. https://doi.org/10.1016/j.soilbio.2024.109596

Vienne, A., Cox, T., Niron, H., Guenet, B., Poetra, R., Steinwidder, L., et al. (2026). Integrating Experiments and Models To Unravel Interactions between Soil Organic Matter and Enhanced Weathering. *Environmental Science & Technology*, acs.est.6c00236. https://doi.org/10.1021/acs.est.6c00236

Vienne, A., Frings, P., Rijnders, J., Boito, L., Hartmann, J., Niron, H., et al. (2026). Weathering without realizing inorganic CO_2 removal revealed through base cation monitoring. *SOIL*, *12*(1), 421–440. https://doi.org/10.5194/soil-12-421-2026

Wang, J., Bouchez, J., Winnick, M. J., Goodwell, A. E., Dere, A., Kumar, P., & Druhan, J. L. (2025). Drought constrictions on lateral carbon transport. *Nature Geoscience*, *18*(11), 1138–1143. https://doi.org/10.1038/s41561-025-01807-z

Zeng, S., Kaufmann, G., & Liu, Z. (2022). Natural and Anthropogenic Driving Forces of Carbonate Weathering and the Related Carbon Sink Flux: A Model Comparison Study at Global Scale. *Global Biogeochemical Cycles*, *36*(3), e2021GB007096. https://doi.org/10.1029/2021GB007096

Zhang, B., Kroeger, J., Planavsky, N., & Yao, Y. (2023). Techno-Economic and Life Cycle Assessment of Enhanced Rock Weathering: A Case Study from the Midwestern United States. *Environmental Science & Technology*, *57*(37), 13828–13837. https://doi.org/10.1021/acs.est.3c01658

Zhao, M., & Running, S. W. (2010). Drought-induced reduction in global terrestrial net primary production from 2000 through 2009. *Science*, *329*(5994), 940–943. https://doi.org/10.1126/science.1192666

Zhao, M., Heinsch, F. A., Nemani, R. R., & Running, S. W. (2005). Improvements of the MODIS terrestrial gross and net primary production global data set. *Remote Sensing of Environment*, *95*(2), 164–176. https://doi.org/10.1016/j.rse.2004.12.011